

Octree-Based Shifted Boundary Method for Multiphysics Simulations Using Linearized Navier-Stokes in Complex Geometries

Cheng-Hau Yang^a, Guglielmo Scovazzi^b, Adarsh Krishnamurthy^a, Baskar Ganapathysubramanian^{a,*}

^aIowa State University, Ames, IA

^bDepartment of Civil and Environmental Engineering, Duke University, Durham, North Carolina 27708, USA

Abstract

This paper presents the application of the Shifted Boundary Method (SBM) to thermal flow simulations, utilizing incomplete octree meshes (Octree-SBM) to perform multiphysics simulations that couple flow and heat transfer. By employing a linearized form of the Navier-Stokes equations, we accelerate the simulations while maintaining accuracy. SBM enables precise enforcement of field and derivative boundary conditions on intercepted elements, allowing for accurate flux calculations near complex geometries, when using non-boundary fitted meshes. Both Dirichlet and Neumann boundary conditions are implemented within the SBM framework, with results demonstrating that SBM ensures precise enforcement of Neumann boundary conditions on octree-based meshes. We illustrate this approach by simulating flows across different regimes, benchmarking results over several orders of magnitude variation in Rayleigh numbers ($Ra \sim 10^3$ to 10^9) and Reynolds numbers ($Re \sim 10^0$ to 10^4), covering laminar, transitional, and turbulent regimes. Coupled thermal-flow phenomena as well as summary statistics across all these regimes are accurately captured without any additional numerical treatments, beyond a Residual-based Variational Multiscale formulation (RB-VMS). This approach offers a reliable and efficient solution for complex geometries, boundary conditions and flow regimes in computational multiphysics simulations.

Keywords: Shifted Boundary Method; Immersed Boundary Method; Computational fluid dynamics; Incomplete octree; Optimal surrogate boundary; Weak boundary conditions; Buoyancy-driven convection; Residual-based variational multiscale

1. Introduction

Natural and forced convection are fundamental mechanisms in heat transfer, influencing a wide range of engineering applications. These processes are essential for optimizing the design of thermal exchangers [1, 2]. Beyond industrial contexts, convection plays a key role in addressing climate-related challenges. For example, the urban heat island effect has become increasingly prominent due to rising global temperatures and urbanization, making the understanding and management of convection more critical than ever [3, 4]. In sustainable building design, natural ventilation has emerged as a promising strategy for improving energy efficiency by harnessing wind and thermal energy [5, 6]. Furthermore, accurately modeling the interaction between airflow and temperature in built environments is essential for ensuring indoor comfort and safety. This is particularly relevant in the context of public health, where effective airflow control is crucial in preventing the spread of infectious diseases [7–12].

Simulating these processes, however, often involves geometrically complex domains, such as urban layouts in heat island studies, human anatomy in aerosolized virus transmission modeling, or intricate configurations in thermal exchangers. Generating boundary-fitted meshes for such geometries is time-consuming and resource-intensive. Moreover, during simulations, engineers frequently discover that some regions require finer resolution, while others can afford coarser discretization. Adjusting these resolutions typically necessitates revisiting meshing software like

*Corresponding authors

Email addresses: chenghau@iastate.edu (Cheng-Hau Yang), guglielmo.scovazzi@duke.edu (Guglielmo Scovazzi), adarsh@iastate.edu (Adarsh Krishnamurthy), baskarg@iastate.edu (Baskar Ganapathysubramanian)

Gmsh or commercial tools (e.g., ANSYS Meshing), which is impractical for workflows demanding rapid iterations, such as those required for building large datasets in the era of AI-driven research [13], or during the design process.

The immersed boundary method (IBM) [14–20] offers an alternative by enabling the use of non-boundary-fitted meshes, significantly simplifying the meshing process. This approach decouples the computational grid from geometric complexity, allowing researchers to perform simulations and testing with greater efficiency. However, traditional IBM implementations, such as the Finite Cell Method (FCM) [21–26] and immersogeometric analysis (IMGA) [27–36], face inherent challenges. Issues such as the small-cut cell (or Intercepted element) problem and load balancing inefficiencies arise because elements intersected by the geometry often require a disproportionately large number of integration points, leading to uneven computational loads across processors.

To address these limitations, recent advancements in IBM have proposed integrating over a surrogate domain instead of directly working on the cut elements (or Intercepted elements). This innovation forms the basis of the Shifted Boundary Method (SBM) [10, 37–47], which has demonstrated notable success across various applications. SBM has demonstrated its versatility in various applications, including fluid dynamics [48], structural simulations [41], free surface flows [49], and one-way coupled fluid-structure interaction (FSI) [50]. By eliminating the need for boundary-fitted meshing, SBM significantly reduces preprocessing time while maintaining high accuracy. However, efficiently and automatically generating non-boundary-fitted meshes for SBM or IBM simulations remains challenging. To overcome this, there have been recent efforts to employ octree meshes, which enable faster and parallelized generation of non-boundary-fitted meshes. Octree meshes stand out due to their favorable aspect ratios, intrinsic hierarchical structure, and compatibility with parallel computing frameworks [51–58, 58–64]. These properties minimize inter-processor communication overhead by localizing the required neighborhood element information, making them highly efficient for large-scale, distributed simulations. The Octree-SBM framework, which combines octree meshes with the SBM, has been applied to a variety of PDEs [47, 65]. Together, they provide robust capabilities for handling geometrically complex domains while maintaining computational efficiency and accuracy, making them a promising approach for modern simulation challenges.

Modeling thermal flows using SBM is, therefore, a promising avenue for a variety of applications, but has been largely unexplored. Existing research has been limited to a single example involving a 1D convection-diffusion equation [37]. Motivated by this gap, this paper investigates the efficacy of SBM for thermal incompressible flow simulations, with a focus on a coupled solver framework for the Navier-Stokes and convection-diffusion equations. The simulation framework developed in this study leverages octree discretization, the linearized Navier-Stokes equations using a Variational Multiscale (VMS) formulation, a two-way coupling mechanism between the Navier-Stokes equations and heat transfer, backflow stabilization techniques for both Navier-Stokes and convection-diffusion equations, and the implementation of SBM for efficiently handling complex geometries. This comprehensive approach enables accurate and efficient simulations of thermal incompressible flows, addressing key challenges in both computational efficiency and geometric flexibility. Our key contributions are:

- *Application of SBM for thermal flow simulations:* Shifted Boundary Method (SBM) with octree-based discretization for efficient handling of complex geometries.
- *Linearized Navier-Stokes and Heat Transfer (NS-HT) solver:* A linearized solver framework for fast and accurate solutions in coupled thermal flow simulations.
- *Comprehensive validation:* Validate the framework across diverse geometries in 2D and 3D, spanning multiple flow regimes and boundary conditions.

This paper is structured as follows: In [Section 2](#), we present the equations we solve, which are divided into the Navier-Stokes subproblem and the Heat Transfer subproblem. In [Section 3](#), we discuss the coupling of Navier-Stokes and Heat Transfer, introducing the block-iterative strategy. In [Section 4](#), we perform various simulations, including both 2D and 3D cases; mixed, forced, and natural convection; and scenarios with Neumann and Dirichlet boundary conditions. Finally, in [Section 5](#), we summarize our findings and suggest directions for future work.

2. Mathematical Formulation

2.1. Formulation for linearized Navier Stokes

The strong form of the non-dimensional Navier-Stokes equations can be written as follow:

$$\text{Momentum Eqns: } \frac{\partial u_i}{\partial t} + u_j \frac{\partial u_i}{\partial x_j} - \nu \frac{\partial^2 u_i}{\partial x_j^2} + \frac{\partial p}{\partial x_i} - f_i = 0. \quad (1)$$

$$\text{Continuity Eqn: } \frac{\partial u_i}{\partial x_i}. \quad (2)$$

The ν in the momentum equations can be written in natural, forced, and mixed convection situations:

$$\nu = \begin{cases} \sqrt{\frac{Pr}{Ra}} = \sqrt{\frac{1}{Gr}}, & \text{Natural convection;} \\ \frac{1}{Re}, & \text{Forced or mixed convection,} \end{cases} \quad (3)$$

where $Ra = \frac{\hat{g}\beta\Delta T L_0^3}{\nu\alpha}$ is the Rayleigh number, $Gr = \frac{\hat{g}\beta\Delta T L_0^3}{\nu^2}$ is the Grashof number, $Pr = \frac{\nu}{\alpha}$ is the Prandtl number, and $Re = \frac{\rho u_0 L_0}{\mu}$ is the Reynolds number. Here, \hat{g} denotes the acceleration due to gravity, β is the coefficient of thermal expansion, and $\Delta T = T_h - T_c$ represents the temperature difference between the highest temperature (T_h) and the lowest temperature (T_c). The parameter L_0 is the characteristic length scale of the system, μ is the dynamic viscosity, α is the thermal diffusivity, ρ is the density of the fluid.

We consider an implicit, second-order accurate in time discretization of $\frac{\partial u_i}{\partial t}$. We utilize the Backward Difference Formula (BDF) discretization of the time derivatives. Unlike our previous work, here, we consider the possibility that successive time-steps, $\Delta t^n = t^{n+1} - t^n$ and $\Delta t^{n-1} = t^n - t^{n-1}$, are not necessarily equal, thus allowing the possibility of variable time stepping. Due to these variable time steps, the time derivative term $\frac{\partial u_i^{n+1}}{\partial t}$ can be expressed (using a backward difference formula (specifically, BDF2)):

$$\frac{\partial u_i^{n+1}}{\partial t} \approx \gamma_0 u_i^{n+1} + \gamma_1 u_i^n + \gamma_2 u_i^{n-1},$$

where coefficients γ_0 , γ_1 , and γ_2 are provided in [Table 1](#). This produces a second order accurate in time discretization, which is implicit in the unknown variable. We use the method of manufactured solutions (MMS) to evaluate accuracy while using the coefficients listed in [Table 1](#), as detailed in [Appendix A.1](#). These simulations highlight the importance of applying the correct BDF2 coefficients when using variable time steps. The rationale for testing variable time steps is grounded in the practical considerations of CFD simulations. Users of our framework may often prefer to gradually increase the Reynolds number through a ramping approach. This strategy helps the solution converge more reliably, reducing the risk of numerical instabilities that could arise from an abrupt jump to high Reynolds numbers. At lower Reynolds numbers, larger time steps are typically sufficient and can enhance computational efficiency. However, as the Reynolds number increases, smaller time steps are preferred to maintain numerical stability and accuracy, ensuring robust simulation performance across a range of flow conditions. Additionally, this approach allows natural extension to adaptive time-stepping.

Table 1: Coefficients for the BDF2 (second order in time) and Backward Euler (BDF1, first order in time) implicit methods are provided, along with BDF2 coefficients for non-uniform timesteps. The validation results using the non-uniform timestep BDF2 coefficients are presented in [Figure A.3](#).

	γ_0	γ_1	γ_2
BDF2, non-uniform Δt	$\frac{1}{\Delta t^n} \left(1 + \frac{\Delta t^n}{\Delta t^n + \Delta t^{n-1}} \right)$	$-\frac{\Delta t^n + \Delta t^{n-1}}{\Delta t^n \Delta t^{n-1}}$	$\frac{1}{\Delta t^{n-1}} \left(\frac{\Delta t^n}{\Delta t^n + \Delta t^{n-1}} \right)$
BDF2, uniform Δt	$\frac{3}{2\Delta t}$	$-\frac{2}{\Delta t}$	$\frac{1}{2\Delta t}$
BE (BDF1)	$\frac{1}{\Delta t^n}$	$-\frac{1}{\Delta t^n}$	0

Before defining the variational formulations, we introduce the scalar and vector discrete function spaces as follows:

$$\tilde{V}^h(\tilde{\Omega}_h^\lambda) = \{q^h \mid q^h \in C^0(\Omega) \cap \mathcal{P}^1(T), \text{ with } T \in \tilde{\mathcal{T}}_h^\lambda\}, \quad (4)$$

$$\tilde{V}^h(\tilde{\Omega}_h^\lambda) = \{Mw \mid Mw \in (C^0(\Omega))^d \cap (\mathcal{P}^1(T))^d, \text{ with } T \in \tilde{\mathcal{T}}_h^\lambda\}. \quad (5)$$

The weak form of the governing equations, incorporating Variational Multiscale Stabilization (VMS) terms, can be written as follows:

Find $u_i \in V^h(\Omega)$ and $p \in V^h(\Omega)$, such that, for any $w_i \in V^h(\Omega)$ and $q \in V^h(\Omega)$,

$$\begin{aligned} \text{Momentum: } & \underbrace{\left(w_i, \gamma_0 u_i^{c,n+1} + \gamma_1 u_i^{c,n} + \gamma_2 u_i^{c,n-1}\right)_{\tilde{\Omega}_h}}_{\text{Time derivative term}} + \underbrace{\left(w_i, u_j^* \frac{\partial u_i^{c,n+1}}{\partial x_j}\right)_{\tilde{\Omega}_h}}_{\text{Coarse convection term}} - \underbrace{\left(u_j^* \frac{\partial w_i}{\partial x_j}, u_i^{f,n+1}\right)_{\tilde{\Omega}_h}}_{\text{Fine convection term}} \\ & + \underbrace{\nu \left(\frac{\partial w_i}{\partial x_j}, \frac{\partial u_i^{c,n+1}}{\partial x_j}\right)_{\tilde{\Omega}_h}}_{\text{Diffusion term}} - \underbrace{\left(\frac{\partial w_i}{\partial x_i}, p^{c,n+1}\right)_{\tilde{\Omega}_h}}_{\text{Coarse pressure term}} - \underbrace{\left(\frac{\partial w_i}{\partial x_i}, p_i^{f,n+1}\right)_{\tilde{\Omega}_h}}_{\text{Fine pressure term}} - \underbrace{\left(w_i, f_i^{n+1}\right)_{\tilde{\Omega}_h}}_{\text{Forcing term}} = 0, \end{aligned} \quad (6)$$

$$\text{Continuity: } \underbrace{\left(q, \frac{\partial u_i^{c,n+1}}{\partial x_i}\right)_{\tilde{\Omega}_h}}_{\text{Coarse scale}} - \underbrace{\left(\frac{\partial q}{\partial x_i}, u_i^{f,n+1}\right)_{\tilde{\Omega}_h}}_{\text{Fine scale}} = 0, \quad (7)$$

where

$$\begin{aligned} u_i^{f,n+1} &= -\tau_m(u_i^{c,n+1})r_M(u_i^{c,n+1}, p^{c,n+1}) \\ &= -\tau_m(u_i^{c,n+1}) \left(\underbrace{\left(\gamma_0 u_i^{c,n+1} + \gamma_1 u_i^{c,n} + \gamma_2 u_i^{c,n-1}\right)}_{\text{BDF2}} + u_j^* \frac{\partial u_i^{c,n+1}}{\partial x_j} - \nu \frac{\partial^2 u_i^{c,n+1}}{\partial x_j^2} + \frac{\partial p^{c,n+1}}{\partial x_i} - f_i^{n+1} \right) \end{aligned} \quad (8)$$

$$p_i^{f,n+1} = -\tau_c r_C(u_i^{c,n+1}) = -\tau_c \left(\frac{\partial u_i^{c,n+1}}{\partial x_i} \right) \quad (9)$$

$$u_i^n = u_i^{c,n} + u_i^{f,n} = u_i^{c,n} - \tau_m(u_i^{c,n}) \left(\underbrace{\left(\gamma_0 u_i^{c,n} + \gamma_1 u_i^{c,n-1} + \gamma_2 u_i^{c,n-2}\right)}_{\text{BDF2}} + u_j^* \frac{\partial u_i^{c,n}}{\partial x_j} - \nu \frac{\partial^2 u_i^{c,n}}{\partial x_j^2} + \frac{\partial p^{c,n}}{\partial x_i} - f_i^n \right) \quad (10)$$

$$u_i^{n-1} = u_i^{c,n-1} + u_i^{f,n-1} = u_i^{c,n-1} - \tau_m(u_i^{c,n-1}) \left(\underbrace{\left(\gamma_0 u_i^{c,n-1} + \gamma_1 u_i^{c,n-2}\right)}_{\text{BDF1}} + u_j^* \frac{\partial u_i^{c,n-1}}{\partial x_j} - \nu \frac{\partial^2 u_i^{c,n-1}}{\partial x_j^2} + \frac{\partial p^{c,n-1}}{\partial x_i} - f_i^{n-1} \right) \quad (11)$$

$$u_i^* = \frac{(\Delta t_{n-1} + \Delta t_n)u_i^n - \Delta t_n u_i^{n-1}}{\Delta t_{n-1}} \quad (12)$$

and

$$\tau_m = \left(\frac{4}{\Delta t^2} + u_j G_{ij} u_i + \frac{C_M}{Re^2} G_{ij} G_{ij} \right)^{-\frac{1}{2}} \quad (13)$$

$$\tau_c = (\tau_M g_j g_j)^{-1} \quad (14)$$

$$G_{ij} = \frac{\partial \xi_k}{\partial x_i} \frac{\partial \xi_k}{\partial x_j} \quad (15)$$

$$g_i = \sum_{j=1}^d \frac{\partial \xi_j}{\partial x_i} \quad (16)$$

C_M and C_E are chosen as 36. The quantities G_{ij} and g_i are related to mapping physical elements to their isoparametric elements.

Inside the formulations (Eq. 6 and Eq. 7), the uppercase letters c and f are used to distinguish the coarse and fine scale variables, respectively. The superscripts $n + 1$, n , and $n - 1$ following c and f denote the time steps of the simulation: $n + 1$ corresponds to the time step being solved, n represents the current time step, and $n - 1$ refers to the previous time step. In the convection term discretization (Eq. 6), an approximate velocity (u_i^*) is computed through an extrapolation based on the previous two time steps (u_i^n and u_i^{n-1}), as detailed in equations Eq. 10, Eq. 11, and Eq. 12. This approach enables a linearized Navier-Stokes solver by replacing the nonlinear convective term with a linearized approximation, thereby simplifying the computational solution strategy. The force term varies across three different scenarios:

$$f_i^{n+1} = \begin{cases} \theta^{c,n+1} \delta_{im}, & \text{Natural convection;} \\ 0, & \text{Forced convection;} \\ \frac{Gr}{Re^2} \theta^{c,n+1} \delta_{im} = Ri \theta^{c,n+1} \delta_{im}, & \text{Mixed convection;} \end{cases} \quad (17)$$

where m is the direction of the gravity, θ is the non-dimensional temperature (see next sub-section), Gr is the Grashof number, and Ri is the Richardson number.

2.2. Formulation for convection diffusion equation

The strong form and the boundary conditions for the convection diffusion equation can be written as follows:

$$\frac{\partial \theta}{\partial t} + u_j \frac{\partial \theta}{\partial x_j} - \alpha \frac{\partial^2 \theta}{\partial x_j^2} = 0, \quad (18)$$

where α for natural and forced convection scenarios is given as:

$$\alpha = \begin{cases} \sqrt{\frac{1}{PrRa}}, & \text{Natural convection;} \\ \frac{1}{Pe}, & \text{Forced or mixed convection.} \end{cases} \quad (19)$$

Here, $Pe = Re \times Pr$ represents the Peclet number, where we select $Pr = 0.7$, which corresponds to air. Table 2 shows how ν , f_i , and α are chosen based on different convection types (summarizing Eq. 3, Eq. 17, and Eq. 19). The weak form can be stated as:

Find $\theta \in V^h(\Omega)$, such that $\forall \phi \in V^h(\Omega)$,

$$\underbrace{\left(\phi, \gamma_0 \theta^{c,n+1} + \gamma_1 \theta^{c,n} + \gamma_2 \theta^{c,n-1} \right)_{\hat{\Omega}_h}}_{\text{Time derivative term}} + \underbrace{\left(\phi, u_j^{c,n} \frac{\partial \theta^{c,n+1}}{\partial x_j} \right)_{\hat{\Omega}_h}}_{\text{Convection term}} + \underbrace{\alpha \left(\frac{\partial \phi}{\partial x_j}, \frac{\partial \theta^{c,n+1}}{\partial x_j} \right)_{\hat{\Omega}_h}}_{\text{Diffusion term}} + \underbrace{\tau_{\text{SUPG}} \left(u_j^{c,n} \frac{\partial \phi}{\partial x_j}, \gamma_0 \theta^{c,n+1} + \gamma_1 \theta^{c,n} + \gamma_2 \theta^{c,n-1} + u_j^{c,n+1} \frac{\partial \theta^{c,n+1}}{\partial x_j} \right)_{\hat{\Omega}_h}}_{\text{SUPG term}} = 0. \quad (20)$$

Table 2: Summary of non-dimensional parameters and forcing terms for natural, forced, and mixed convection scenarios.

	Natural	Forced	Mixed
ν	$\sqrt{\frac{Pr}{Ra}} = \sqrt{\frac{1}{Gr}}$	$\frac{1}{Re}$	$\frac{1}{Re}$
α	$\sqrt{\frac{1}{PrRa}}$	$\frac{1}{Pe}$	$\frac{1}{Pe}$
f_i	$\theta^c \delta_{im}$	0	$\frac{Gr}{Re^2} \theta^c \delta_{im} = Ri \theta^c \delta_{im}$

Similar to the Navier-Stokes equations, we consider variable time step in our formulation: $\Delta t^n = t^{n+1} - t^n$ and $\Delta t^{n-1} = t^n - t^{n-1}$, and we use $\gamma_0 \theta^{n+1} + \gamma_1 \theta^n + \gamma_2 \theta^{n-1}$ to approximate $\frac{\partial \theta^{n+1}}{\partial t}$. For the coefficients of the time derivative, we refer to [Table 1](#). To address potential numerical instabilities in advection-dominated problems, we incorporate the Streamline-Upwind Petrov-Galerkin (SUPG) stabilization term [66]. This term is designed to enhance solution stability along the streamlines by introducing additional weighting. For the SUPG term, we neglect the diffusion term given that we use the linear basis function in our framework. The SUPG stabilization parameter τ_{SUPG} is defined as:

$$\tau_{\text{SUPG}} = \frac{hz}{2\sqrt{u_i u_i}}, \quad (21)$$

where u_i is the velocity vector and $\sqrt{u_i u_i}$ its magnitude.

The element length h is:

$$h = \frac{2}{\sum_A \frac{|u_i \frac{\partial N_A}{\partial x_i}|}{\sqrt{u_i u_i}}}, \quad (22)$$

with N_A as the shape function, $\frac{\partial N_A}{\partial x_i}$ its gradient, and A running over all nodes of the element. The parameter z depends on the local Reynolds number:

$$Re_u = \frac{\sqrt{u_i u_i} h}{2\nu}, \quad (23)$$

The value of z is:

$$z = \begin{cases} 1 & \text{if } Re_u > 3, \\ \frac{Re_u}{3} & \text{if } Re_u \leq 3. \end{cases} \quad (24)$$

2.3. SBM preliminaries: The true domain, surrogate domain, and maps

[Figure 1a](#) illustrates a closed region \mathcal{D} , where $\text{clos}(\Omega) \subseteq \mathcal{D}$ (with $\text{clos}(\Omega)$ denoting the *closure* of Ω), along with the family $\mathcal{T}_h(\mathcal{D})$ of admissible, shape-regular discrete decompositions (meshes/grids) of \mathcal{D} . In this study, we specifically focus on octree grids that are aligned with the axes of the Cartesian coordinate system. Each $\mathcal{T}_h(\mathcal{D})$ is then restricted by selecting only those elements $T \in \mathcal{T}_h(\mathcal{D})$ that satisfy the condition:

$$\text{meas}(T \cap \Omega) > (1 - \lambda) \text{meas}(T);, \quad \text{for some } \lambda \in [0, 1];. \quad (25)$$

In other words, these elements are those that intersect with the domain of interest Ω and have an area or volume greater than $1 - \lambda$ of their total area or volume, depending on whether the context is two- or three-dimensional. For example, choosing $\lambda = 0$ selects the elements that are strictly contained in the computational domain Ω (see, e.g., [Figure 1a](#)), choosing $\lambda = 1$ selects the elements that have a non-empty intersection with Ω (see, e.g., [Figure 1b](#)), and choosing $\lambda = 0.5$ selects elements whose intersection with Ω includes at least 50% of their area/volume.

We define the family of grids that satisfies [Eq. 25](#) as

$$\tilde{\mathcal{T}}_h^\lambda := \{T \in \mathcal{T}_h(\mathcal{D}) : \text{meas}(T \cap \Omega) > (1 - \lambda) \text{meas}(T)\}.$$

This identifies the *surrogate domain*

$$\tilde{\Omega}_h^\lambda := \text{int} \left(\bigcup_{T \in \tilde{\mathcal{T}}_h^\lambda} T \right),$$

or, more simply, $\tilde{\Omega}_h$, with *surrogate boundary* $\tilde{\Gamma}_h := \partial \tilde{\Omega}_h$ and outward-oriented unit normal vector $\tilde{\mathbf{n}} \rightarrow \tilde{\Gamma}_h$. Obviously, $\tilde{\mathcal{T}}_h^\lambda$ is an admissible and shape-regular family of decompositions of $\tilde{\Omega}_h$ (see again [Figure 1a](#)). Here, we choose $\lambda = 1$, which is advantageous for thermal incompressible flow calculations, particularly for cases where the quantity of interest is the boundary thermal flux, or in dimensionless terms, the Nusselt number, which requires the first derivative at the cut (or INTERCEPTED) element. By selecting $\lambda = 1$, no special implementation is needed to compute the first derivative at the cut (or INTERCEPTED) element. Instead, we can directly use the derivative of the shape function and nodal point values to interpolate and obtain the derivative on the true boundary (Γ).

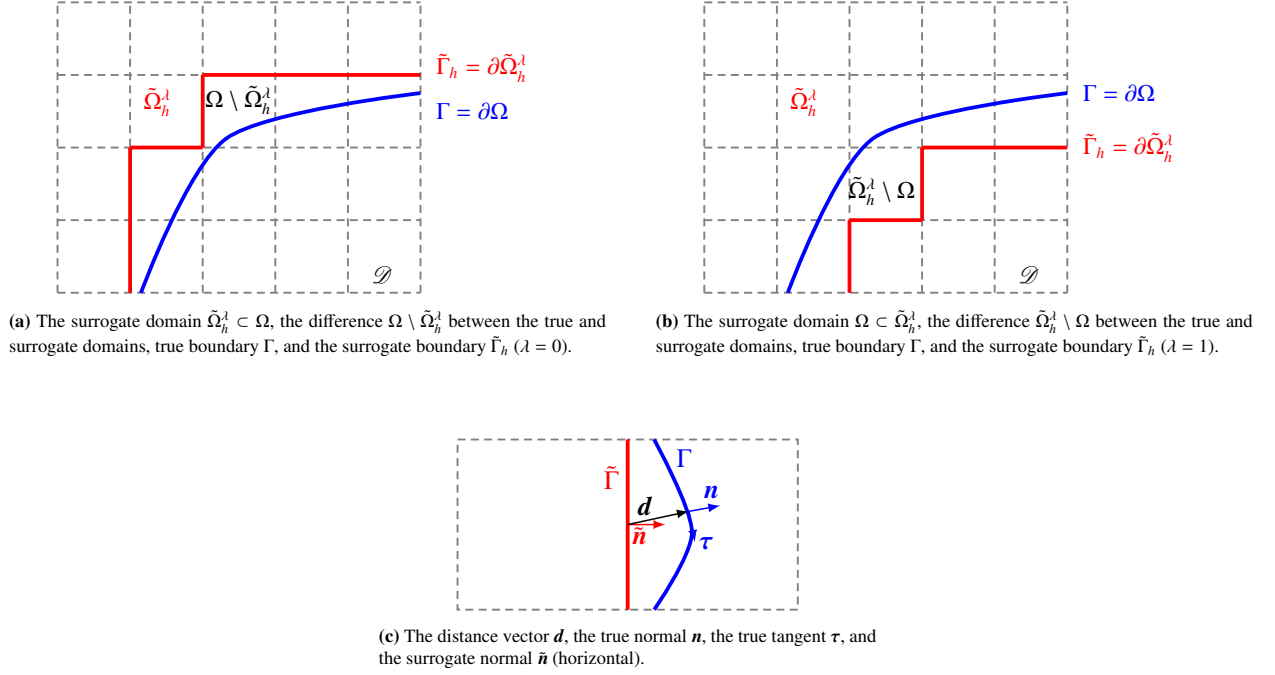


Figure 1: The surrogate domain, its boundary, and the distance vector \mathbf{d} .

The mapping sketched in Figure 1c is defined as follows:

$$\mathbf{M}_h : \tilde{\Gamma}_h \rightarrow \Gamma, \quad (26a)$$

$$\tilde{\mathbf{x}} \mapsto \mathbf{x}, \quad (26b)$$

where \mathbf{M}_h maps any point $\tilde{\mathbf{x}} \in \tilde{\Gamma}_h$ on the surrogate boundary to a point $\mathbf{x} = \mathbf{M}_h(\tilde{\mathbf{x}})$ on the physical boundary Γ .

In this study, \mathbf{M}_h is defined as the closest-point projection of $\tilde{\mathbf{x}}$ onto Γ , as illustrated in Figure 1c. Using this mapping, a distance vector function $\mathbf{d}_{\mathbf{M}_h}$ can be expressed as:

$$\mathbf{d}_{\mathbf{M}_h}(\tilde{\mathbf{x}}) = \mathbf{x} - \tilde{\mathbf{x}} = [\mathbf{M} - \mathbf{I}](\tilde{\mathbf{x}}), \quad (27)$$

where \mathbf{M} is the mapping operator, and \mathbf{I} is the identity operator. For simplicity, we denote $\mathbf{d} = \mathbf{d}_{\mathbf{M}_h}$ and further decompose it as:

$$\mathbf{d} = \|\mathbf{d}\| \mathbf{v},$$

where $\|\mathbf{d}\|$ is the magnitude of the distance vector, and \mathbf{v} is a unit vector indicating the direction of the distance.

Remark. There are several strategies to define the mapping \mathbf{M}_h and, consequently, the distance vector \mathbf{d} . The closest-point projection of $\tilde{\mathbf{x}}$ onto Γ is a natural and widely used choice for determining \mathbf{x} (and thus \mathbf{M}_h), provided it is uniquely defined. However, alternative approaches may be more suitable in specific scenarios. For example, a level-set representation of the true boundary can be employed, where \mathbf{d} is defined using a distance function. For algorithms related to distance functions for complex geometries in 3D, see [47]. For further discussions, including considerations for domains with corners, refer to [41, 42].

2.4. Shifted boundary conditions

We begin by examining Dirichlet boundary conditions, which are particularly relevant as they encompass the no-slip boundary condition - a crucial constraint for fluid-solid interfaces.

Let us consider a surrogate Dirichlet boundary $\tilde{\Gamma}_D$ positioned near the actual Dirichlet boundary Γ_D . By utilizing the distance measure between these boundaries, we can express the velocity vector through its Taylor expansion:

$$\mathbf{u}(\tilde{\mathbf{x}}) + (\nabla \mathbf{u} \cdot \mathbf{d})(\tilde{\mathbf{x}}) + (\mathbf{R}_D(\mathbf{u}, \mathbf{d}))(\tilde{\mathbf{x}}) = \mathbf{u}_D(\mathbf{M}_h(\tilde{\mathbf{x}})), \quad \text{on } \tilde{\Gamma}_{D,h}, \quad (28)$$

Here, the remainder term $\mathbf{R}_D(\mathbf{u}, \mathbf{d})$ exhibits the property that $\|\mathbf{R}_D(\mathbf{u}, \mathbf{d})\| = o(\|\mathbf{d}\|^2)$ as $\|\mathbf{d}\| \rightarrow 0$. To formalize this relationship, we introduce two key operators on $\tilde{\Gamma}_{D,h}$:

The *extension* operator:

$$\mathbb{E}\mathbf{u}_D(\tilde{\mathbf{x}}) := \mathbf{u}_D(\mathbf{M}_h(\tilde{\mathbf{x}})) \quad (29)$$

The *shift* operator:

$$\mathbf{S}_{D,h} \mathbf{u}(\tilde{\mathbf{x}}) := \mathbf{u}(\tilde{\mathbf{x}}) + \nabla \mathbf{u}(\tilde{\mathbf{x}}) \mathbf{d}(\tilde{\mathbf{x}}). \quad (30)$$

By disregarding the higher-order residual term in Eq. 28, we arrive at the definitive form of the *shifted* boundary conditions:

$$\mathbf{S}_{D,h} \mathbf{u} = \mathbb{E}\mathbf{u}_D, \quad \text{on } \tilde{\Gamma}_{D,h}. \quad (31)$$

2.5. SBM formulation for the linearized Navier-Stokes equations

Suppose the Dirichlet boundary conditions for Navier-Stokes equations are:

$$u_i = g_i \quad \text{on } \Gamma_u^D. \quad (32)$$

Here we use lowercase u in Γ_u^D to distinguish the Navier-Stokes boundary conditions from the convection-diffusion boundary conditions. After plugging in Eq. 8 and Eq. 9 into Eq. 6 and Eq. 7, and adding the boundary terms from SBM to enforce the Dirichlet boundary condition, we can rearrange the equations. By placing the unknowns $(u_i^{c,n+1}, p^{c,n+1})$ on the left-hand side and the known values on the right-hand side, we obtain the following weak form: Find $u_i \in \tilde{V}^h(\tilde{\Omega}_h^\lambda)$ and $p \in \tilde{V}^h(\tilde{\Omega}_h^\lambda)$, such that, for any $w_i \in \tilde{V}^h(\tilde{\Omega}_h^\lambda)$ and $q \in \tilde{V}^h(\tilde{\Omega}_h^\lambda)$,

$$\begin{aligned} & \left(w_i, \gamma_0 u_i^{c,n+1} \right)_{\tilde{\Omega}_h} + \left(w_i, u_j^* \frac{\partial u_i^{c,n+1}}{\partial x_j} \right)_{\tilde{\Omega}_h} + \tau_m \left(u_j^* \frac{\partial w_i}{\partial x_j}, \gamma_0 u_i^{c,n+1} + u_j^* \frac{\partial u_i^{c,n+1}}{\partial x_j} - v \frac{\partial^2 u_i^{c,n+1}}{\partial x_j^2} + \frac{\partial p^{c,n+1}}{\partial x_i} \right)_{\tilde{\Omega}_h} + v \left(\frac{\partial w_i}{\partial x_j}, \frac{\partial u_i^{c,n+1}}{\partial x_j} \right)_{\tilde{\Omega}_h} \\ & - \left(\frac{\partial w_i}{\partial x_i}, p^{c,n+1} \right)_{\tilde{\Omega}_h} + \tau_c \left(\frac{\partial w_i}{\partial x_i}, \frac{\partial u_j^{c,n+1}}{\partial x_j} \right)_{\tilde{\Omega}_h} + \left(q, \frac{\partial u_i^{c,n+1}}{\partial x_i} \right)_{\tilde{\Omega}_h} + \tau_m \left(\frac{\partial q}{\partial x_i}, \gamma_0 u_i^{c,n+1} + u_j^* \frac{\partial u_i^{c,n+1}}{\partial x_j} - v \frac{\partial^2 u_i^{c,n+1}}{\partial x_j^2} + \frac{\partial p^{c,n+1}}{\partial x_i} \right)_{\tilde{\Omega}_h} \\ & - \underbrace{\left\langle w_i, v \left(\frac{\partial u_i^{c,n+1}}{\partial x_j} + \frac{\partial u_j^{c,n+1}}{\partial x_i} \right) \tilde{n}_j - p \tilde{n}_i \right\rangle_{\tilde{\Gamma}_{D,h}}}_{\text{Consistency term}} - \underbrace{\left\langle v \left(\frac{\partial w_i}{\partial x_j} + \frac{\partial w_j}{\partial x_i} \right) \tilde{n}_j + q \tilde{n}_i, u_i^{c,n+1} + \frac{\partial u_i^{c,n+1}}{\partial x_j} d_j \right\rangle_{\tilde{\Gamma}_{D,h}}}_{\text{Adjoint consistency term}} \\ & + \underbrace{\frac{C_M^B v}{h} \left\langle w_i + \frac{\partial w_i}{\partial x_j} d_j, u_i^{c,n+1} + \frac{\partial u_i^{c,n+1}}{\partial x_j} d_j \right\rangle_{\tilde{\Gamma}_{D,h}}}_{\text{Penalty term}} \\ & = - \left(w_i, \gamma_1 u_i^{c,n} + \gamma_2 u_i^{c,n-1} \right)_{\tilde{\Omega}_h} - \tau_m \left(u_j^* \frac{\partial w_i}{\partial x_j}, \gamma_1 u_i^{c,n} + \gamma_2 u_i^{c,n-1} - f_i^{n+1} \right)_{\tilde{\Omega}_h} + \left(w_i, f_i^{n+1} \right)_{\tilde{\Omega}_h} \\ & - \tau_m \left(\frac{\partial q}{\partial x_i}, \gamma_1 u_i^{c,n} + \gamma_2 u_i^{c,n-1} - f_i^{n+1} \right)_{\tilde{\Omega}_h} - \underbrace{\left\langle v \left(\frac{\partial w_i}{\partial x_j} + \frac{\partial w_j}{\partial x_i} \right) \tilde{n}_j + q \tilde{n}_i, g_i \right\rangle_{\tilde{\Gamma}_{D,h}}}_{\text{Adjoint consistency term}} + \underbrace{\frac{C_M^B v}{h} \left\langle w_i + \frac{\partial w_i}{\partial x_j} d_j, g_i \right\rangle_{\tilde{\Gamma}_{D,h}}}_{\text{Penalty term}}, \quad (33) \end{aligned}$$

where C_M^B is the penalty parameter for the Navier-Stokes equation.

The step-by-step details of formulating the Shifted Boundary Method (SBM) for the Navier-Stokes equations is presented in [Appendix B](#).

2.6. SBM formulation for the convection diffusion equation

Suppose the boundary conditions in convection-diffusion equation are:

$$\begin{cases} \theta = \theta_D & \text{on } \Gamma_\theta^D, \\ \nabla\theta \cdot n = h_T & \text{on } \Gamma_\theta^N. \end{cases} \quad (34)$$

We utilize SBM to enforce both the Dirichlet and Neumann boundary conditions. By arranging equation with the unknown $(\theta^{c,n+1})$ on the left hand side and the known values on the hand side, we derive the following linear system to solve:

Find $\theta \in \tilde{V}^h(\tilde{\Omega}_h^A)$, such that $\forall \phi \in \tilde{V}^h(\tilde{\Omega}_h^A)$,

$$\begin{aligned} & \left(\phi, \gamma_0 \theta^{c,n+1} \right)_{\tilde{\Omega}_h} + \left(\phi, u_j^{c,n} \frac{\partial \theta^{c,n+1}}{\partial x_j} \right)_{\tilde{\Omega}_h} + \alpha \left(\frac{\partial \phi}{\partial x_j}, \frac{\partial \theta^{c,n+1}}{\partial x_j} \right)_{\tilde{\Omega}_h} + \tau_{\text{SUPG}} \left(u_j^{c,n} \frac{\partial \phi}{\partial x_j}, \gamma_0 \theta^{c,n+1} + u_j^{c,n+1} \frac{\partial \theta^{c,n+1}}{\partial x_j} \right)_{\tilde{\Omega}_h} \\ & + \underbrace{\alpha \left\langle \phi, (\tilde{n}_j n_j) \frac{\partial \theta^{c,n+1}}{\partial x_j} n_j \right\rangle_{\tilde{\Gamma}_{N,h}} - \alpha \left\langle \phi, \frac{\partial \theta^{c,n+1}}{\partial x_j} \tilde{n}_j \right\rangle_{\tilde{\Gamma}_{N,h}} - \alpha \left\langle \phi, \frac{\partial \theta^{c,n+1}}{\partial x_j} \tilde{n}_j \right\rangle_{\tilde{\Gamma}_{D,h}} - \alpha \left\langle \frac{\partial \phi}{\partial x_j} \tilde{n}_j, \theta^{c,n+1} + \frac{\partial \theta^{c,n+1}}{\partial x_j} d_j \right\rangle_{\tilde{\Gamma}_{D,h}}}_{\text{SBM neumann term}} \\ & + \underbrace{\frac{C_E^B \alpha}{h} \left\langle \phi + \frac{\partial \phi}{\partial x_j} d_j, \theta^{c,n+1} + \frac{\partial \theta^{c,n+1}}{\partial x_j} d_j \right\rangle_{\tilde{\Gamma}_{D,h}}}_{\text{Penalty term}} \\ & = - \left(\phi, \gamma_1 \theta^{c,n} + \gamma_2 \theta^{c,n-1} \right)_{\tilde{\Omega}_h} - \tau_{\text{SUPG}} \left(u_j^{c,n} \frac{\partial \phi}{\partial x_j}, \gamma_1 \theta^{c,n} + \gamma_2 \theta^{c,n-1} \right)_{\tilde{\Omega}_h} + \underbrace{\alpha \left\langle \phi, (\tilde{n}_j n_j) h_T \right\rangle_{\tilde{\Gamma}_{N,h}}}_{\text{SBM neumann term}} \\ & - \underbrace{\alpha \left\langle \frac{\partial \phi}{\partial x_j} \tilde{n}_j, \theta_D \right\rangle_{\tilde{\Gamma}_{D,h}}}_{\text{Adjoint consistency term}} + \underbrace{\frac{C_E^B \alpha}{h} \left\langle \phi + \frac{\partial \phi}{\partial x_j} d_j, \theta_D \right\rangle_{\tilde{\Gamma}_{D,h}}}_{\text{Penalty term}}, \end{aligned} \quad (35)$$

where C_E^B is the penalty parameter for the convection-diffusion equation.

2.7. Backflow stabilization

Instabilities arising from backflow at outflow or open boundaries can lead to solver divergence in thermal incompressible flow simulations. Backflow stabilization introduces a dissipative boundary term that activates in the presence of backflow, effectively maintaining stability. This approach is particularly suitable for simulations involving thermal incompressible flow problems characterized by strong flow recirculation or vortices impinging on the outlet boundary.

In both the backflow stabilization method [67] and the Directional do-nothing (DDN) boundary condition [68], a boundary term is introduced to the left-hand side of (33):

$$- \left\langle w_i, \beta_0 \min(0, u_j^{c,n} n_j) u_i^{c,n+1} \right\rangle_{\Gamma_o} \quad (36)$$

where β_0 is the stabilization parameter for Navier-Stokes. Similarly, backflow stabilization is applied to the heat transfer equation, adding the following term to the left-hand side of (35):

$$- \left\langle \phi, \beta_\theta \min(0, u_j^{c,n} n_j) \theta^{c,n+1} \right\rangle_{\Gamma_o} \quad (37)$$

where β_θ is the stabilization parameter for heat transfer. In the simulations performed in this paper, we pick $\beta_0 = 0.5$ and $\beta_\theta = 0.5$ for the backflow stabilization terms.

3. Implementation details

3.1. Numerical implementations

Our computational framework is built on two core components: DENDRO-KT [10, 69] and PETSc, both of which play essential roles in enabling high-performance, large-scale scientific simulations across various domains. These tools work together to deliver an efficient and scalable solution for complex numerical problems. At the core of our numerical approach is DENDRO-KT, an in-house open source library that employs octree-based domain decomposition for parallel computing. In prior work, this approach has been applied (in a non-SBM manner) to various multiphysics applications, such as two-phase flow dynamics [70], electrokinetic transport phenomena [71], and computational risk assessments for disease transmission [11]. We employ a block-iterative strategy to couple different PDEs, as mentioned in Section 3.2. Key features include (a) **Complex Geometry Handling using incomplete octrees**: Utilizes in-out tests [19, 59, 72] to efficiently determine point locations within intricate structures, enabling creation of incomplete octrees representing complex geometries. (b) **Adaptive Mesh Refinement**: Ensures high resolution in critical regions (e.g., boundary layers and wake areas) while maintaining computational efficiency. (c) **Load Balancing**: Uses space-filling curves (SFC) to optimally distribute computational tasks across processors in distributed memory environments. (d) **Matrix Assembly**: Streamlines the process through innovative traversal methods, eliminating the need for traditional element mappings. (e) **2:1 Balanced Octrees**: Enhances stability and accuracy by ensuring adjacent octants differ by only one refinement level [69, 73, 74].

Additionally, efficient distance function calculation plays an essential role in the SBM. To address this, we use the k-d tree nanoflann library [75]. For further details on the implementation of these components, readers are referred to Yang et al. [47].

3.2. Block-iterative strategy

The block-iterative strategy has proven to be effective in addressing various multi-physics problems, such as fluid-structure interaction [76], thermal incompressible flow [77], Cahn-Hillard Navier-Stokes coupled two-phase

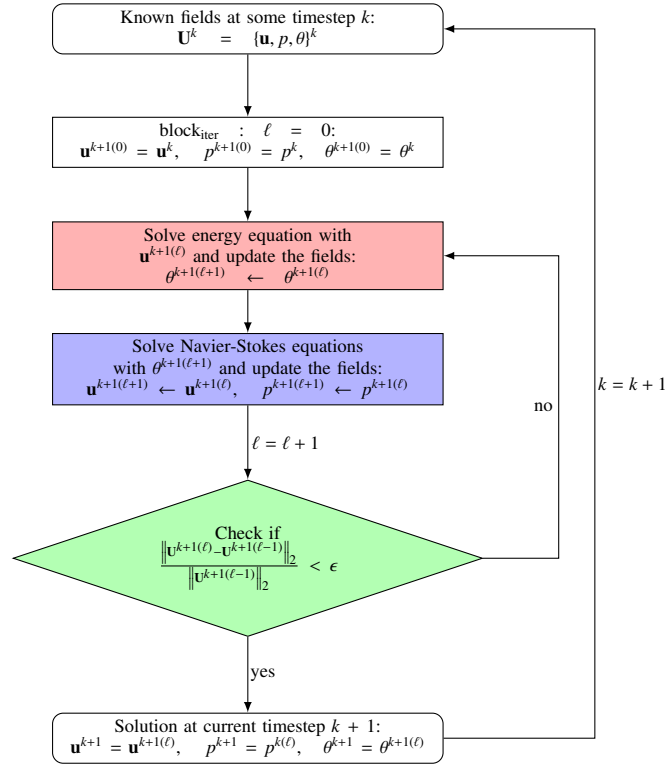


Figure 2: Diagram illustrating the block iteration technique used to perform multiphysics simulations of thermal incompressible flow (NSHT).

flows [70, 78], and thermal free-surface flows [79]. In our framework, we also utilize a block-iterative strategy to couple energy and flow dynamics. The flowchart of this approach is illustrated in Figure 2. Within each block, we solve the convection-diffusion equation, passing the resulting temperature to the Navier-Stokes equation, which is then solved. We check for convergence within the block. If the solution is not convergent, we pass the velocity obtained from solving the Navier-Stokes equation back to the convection-diffusion equation and follow the above loop again. This loop continues until the multi-field solution converges to below a user-defined tolerance.

4. Results

Figure 3 provides a birdseye view of the various scenarios we test the Linearized Octree-SBM approach. Most of the simulation results are displayed in this section, except for the Rayleigh-Bénard results, which are discussed separately in Appendix A.2. Additionally, we performed a numerical study using the method of manufactured solutions to validate the linearized Navier-Stokes solver, as detailed in Appendix A.1.

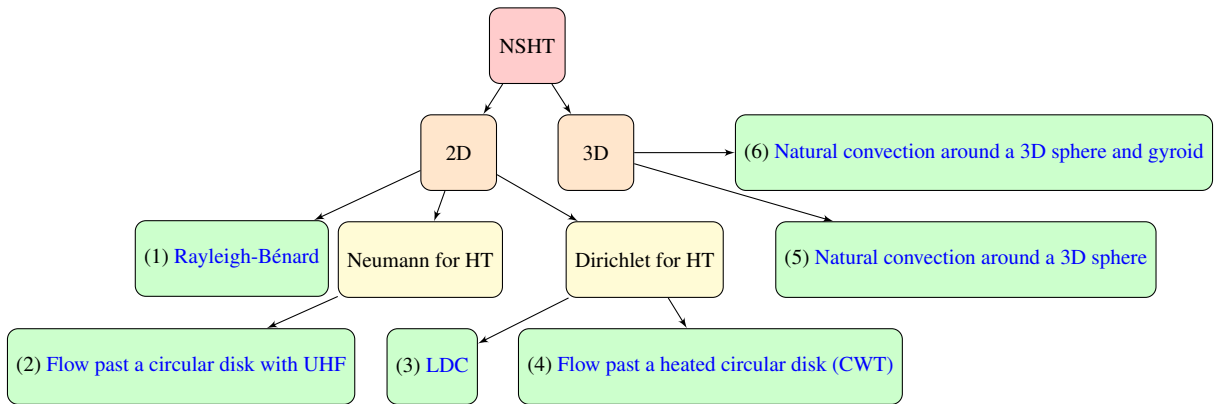


Figure 3: Schematic graph of various NSHT simulations performed in the paper.

4.1. Comparison of running time between Linearized and Non-Linearized Navier-Stokes simulations

To demonstrate the benefit of using the Linearized Navier-Stokes equations in simulations, we selected a canonical problem in incompressible flow: flow past a fixed cylinder in 2D at a Reynolds number of 100. The Navier-Stokes equations are solved using the GMRES (Generalized Minimal Residual) method with a restart value of 1000, coupled with the Additive Schwarz Method (ASM) preconditioner configured with an overlap of 10 on PETSc. The simulations were conducted on the TACC Frontera system, utilizing 10 nodes and a total of 560 processors. The simulation domain is $[0, 30] \times [0, 20]$, featuring a circular disk with a radius of 0.5, positioned at the coordinates (10, 10). A non-dimensional freestream velocity of (1, 0) was applied to all boundary walls, except for the outlet wall, where the pressure was set to zero. Local mesh refinement was applied to ensure sufficient resolution in regions with complex flow behavior. A circular region, centered at (10, 10) with a radius of 1, was refined to level 12 (mesh size = $30 \cdot 2^{-12}$) to capture critical boundary-layer flow features. Additionally, two rectangular refinement regions were used. The first rectangle spans $[8, 14] \times [8, 12]$ and was refined to level 9 (mesh size = $30 \cdot 2^{-9}$). The second rectangle spans $[8, 18] \times [7, 13]$ and was refined to level 8 (mesh size = $30 \cdot 2^{-8}$). These refinement strategies are summarized in Figure 4. We used both Linearized NS and Non-Linearized NS solvers to solve this problem with two different timesteps, 0.01 and 0.002. Our findings indicate that, for the drag coefficient, both solvers yielded consistent results regardless of the time step, as shown in Table 3. For simulations up to the final non-dimensional time of 10, the Linearized Navier-Stokes solver demonstrates superior performance, reducing the total running time by nearly 60% compared to the Non-Linearized Navier-Stokes solver when using a timestep of $\Delta t = 0.002$. The solving time for the Non-Linearized Navier-Stokes equations is used to normalize the solving time for the Linearized Navier-Stokes solver, clearly highlighting the computational efficiency gained by using the Linearized Navier-Stokes approach in Table 4.

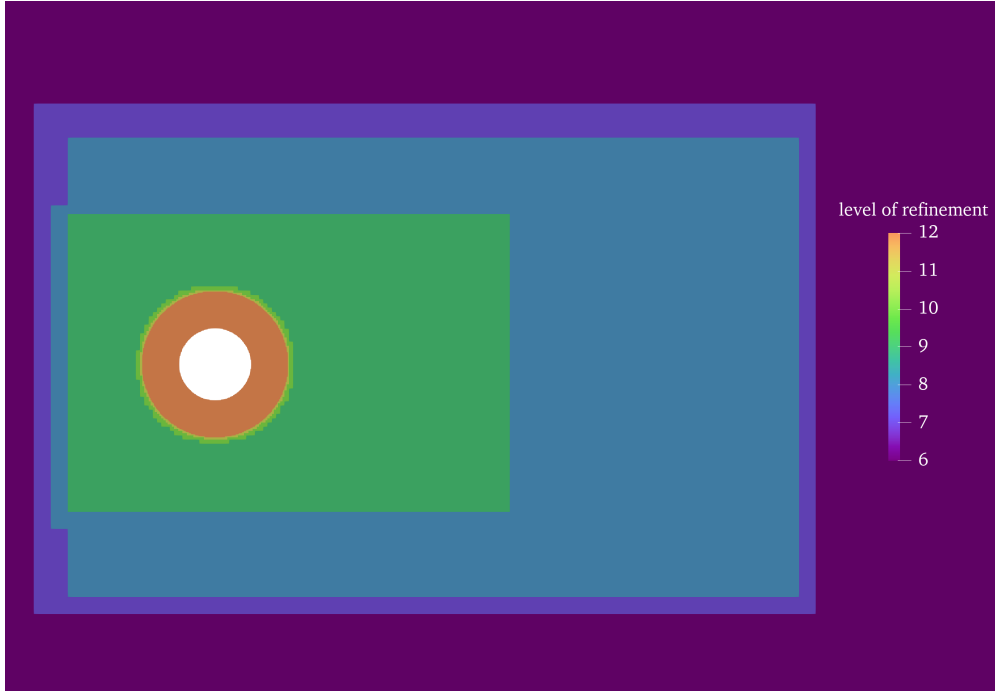


Figure 4: Image showing the various levels of mesh refinement for flow past a circular disk case (Section 4.1). An increase of mesh resolution by 1 represents a reduction in element size by a factor of 2. Here, the finest element and the coarsest element vary by factor of 64 in length (and $64^2 = 4096$ in area)

Table 3: 2D flow past a cylinder case at $Re = 100$. Results using both the linearized as well as non-linear [65] Navier-Stokes frameworks.

Study		Cd
Liu et al. [80]		1.350
Posdziech and Grundmann [81]		1.310
Wu and Shu [82]		1.364
Yang et al. [83]		1.393
Rajani et al. [84]		1.340
Kamensky et al. [85]		1.386
Main and Scovazzi [86] (triangular grid)		1.360
Linearized NS	$\Delta t = 0.01$	1.351
	$\Delta t = 0.002$	1.350
Non-Linearized NS	$\Delta t = 0.01$	1.351
	$\Delta t = 0.002$	1.350

Table 4: Comparison of solving times for Non-Linearized and Linearized Navier-Stokes equations at different time steps.

Time Step (Δt)	NLNS Time (s)	LNS Time (s)	Speed-Up ($\frac{NLNS}{LNS}$)
0.002	1180.0	483.5	2.44
0.010	271.1	136.3	2.00

4.2. Dirichlet boundary condition for heat transfer in 2D

4.2.1. Mixed convection in lid-driven cavity thermal flows

We place circular disks inside the lid-driven cavity and perform simulations of mixed convection, which refers to the combination of natural and forced convection. In this context, the Richardson number (Ri) becomes essential, as it is the non-dimensional number that characterizes the flow regime: when $Ri \ll 1$, the flow is dominated by forced convection; when $Ri \gg 1$, it is dominated by natural convection; and when Ri close to 1, both natural and forced convection contribute significantly. In this study, we conducted two types of simulations: the first involved a single circular disk inside the cavity, and the second involved two circular disks.

In the single-disk simulation, the disk is positioned at the geometric center of a lid-driven cavity, with the cavity having a unit length ($L = 1$). The Dirichlet boundary condition is applied to the disk using SBM, enforcing a non-dimensional temperature of zero and imposing a no-slip boundary condition. The boundary conditions for the problem are detailed in Table 5. The disk has a radius of $0.2L$, where L denotes the length of the cavity. The SBM is used to enforce Dirichlet boundary conditions on the disk for both the Navier-Stokes and energy equations. The non-dimensional parameters used are $Re = 100$, $Pr = 0.7$, and Ri values ranging from 0.01 to 5.0, covering the flow regime from forced convection to mixed convection and natural convection, where $Ri = \frac{Gr}{Re^2}$. For higher Ri values, the flow tends more toward natural convection, while lower Ri values indicate a stronger influence of forced convection. The mesh resolution is 128×128 (mesh size = 2^{-7}).

Table 5: Boundary conditions for mixed convection in lid-driven cavity thermal flows with one circular disk (Section 4.2.1).

Boundary	Navier-Stokes (Velocity)	Heat Transfer (Temperature, θ)
Top Wall	$u = 1, v = 0$	$\theta = 0$
Bottom Wall	$u = 0, v = 0$	$\theta = 1$
Left Wall	$u = 0, v = 0$	Zero flux: $\frac{\partial \theta}{\partial x} = 0$
Right Wall	$u = 0, v = 0$	Zero flux: $\frac{\partial \theta}{\partial x} = 0$

The temperature contours are shown in Figure 5. As Ri increases, the buoyancy effect becomes stronger, causing the high-temperature region to extend further upward in the cavity. Notably, the contour line near the disk region in Figure 5 represents the zero-temperature contour, closely following the shape of the disk. This observation demonstrates that SBM effectively enforces the true boundary condition, even when applied at the surrogate octree-based boundary. To further illustrate this, Figure 6 provides a zoomed-in view of the temperature contour at $Ri = 1$, where the zero-temperature contour (white line) closely matches the circular boundary (red line). Nusselt number comparisons along the bottom wall are presented in Figure 7. Additionally, we compared the temperature profiles along specific lines with data from the literature [87], as shown in Figure 8.

In the next case, we analyze a chamber with two circular disks, as described in [88]. The circular disk on the left is set with a constant non-dimensional temperature of $\theta = 1$ using SBM, while the circular disk on the right is set with a constant non-dimensional temperature of $\theta = 0$ using SBM. The boundary conditions for the walls in the Navier-Stokes equations remain identical to the single circular disk case. The thermal boundary conditions for the rectangular walls are defined such that the temperature θ is set to zero for all boundary walls. Our objective is to accurately capture the Nusselt number at the circular disk regions. To achieve this, we apply local mesh refinement near the circular disks, using a refinement level of 10 (mesh size = 2^{-10}), which creates a refinement region with a radius of 0.23, as shown in Figure 9a. The center of the refinement region coincides with the center of the corresponding geometric circle. The base refinement level is set to 7, corresponding to a mesh size of 2^{-7} . The non-dimensional parameters are $Re = 100$, $Pr = 0.7$, and $Ri = 0.01$ and 10.0. The temperature contours for $Ri = 0.01$ and $Ri = 10$ are presented in Figure 9b and Figure 9c, respectively. The local Nusselt numbers over the circular disks and wall boundaries are illustrated in Figure 10 and Figure 11. In Figure 10, we compare the Nusselt number on the true boundary, which involves calculating the first derivative of our numerical results on the Intercepted elements. These results demonstrate the capability of the SBM to accurately capture the first derivative on the Intercepted elements.

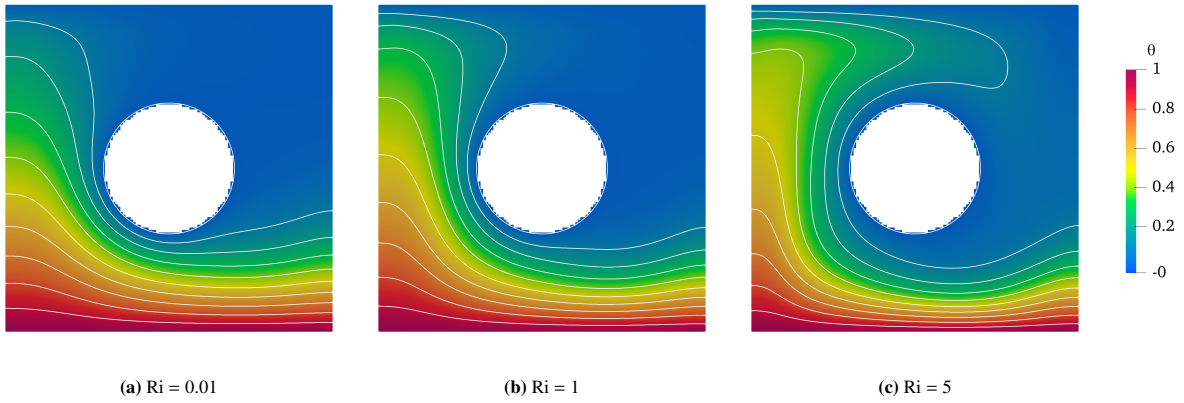


Figure 5: Temperature contour in lid-driven cavity thermal flow case with one circular disk (Section 4.2.1). The contour lines are plotted from 0 to 1 non-dimensional temperature at regular intervals of 0.1.

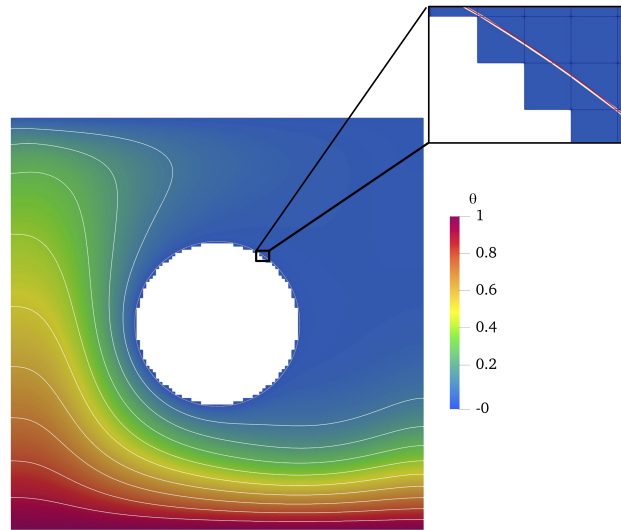


Figure 6: Close-up of the temperature contour in lid-driven cavity flow case (Section 4.2.1) with one circular disk: the red line indicates the geometry boundary, while the white line represents the zero-temperature contour.

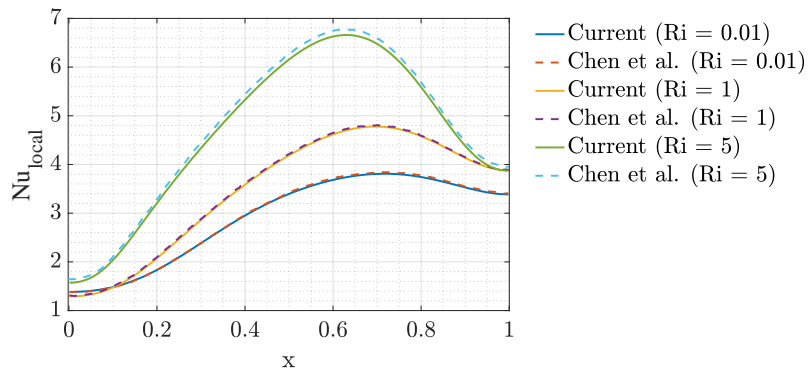


Figure 7: Comparison of the local Nusselt number (non-dimensional thermal flux) with Chen et al. [87] at various locations along the bottom wall for the lid-driven cavity thermal flow case with a circular disk (Section 4.2.1).

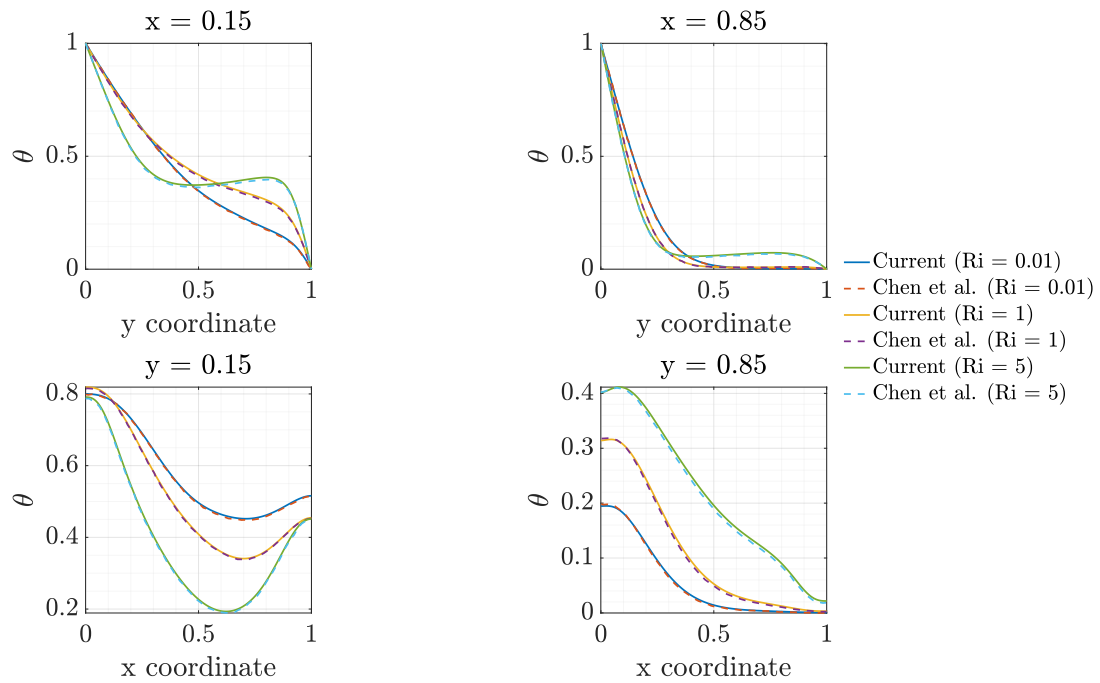


Figure 8: Comparison of temperature distributions with Chen et al. [87] for the lid-driven cavity mixed convection case featuring a circular disk at various Richardson numbers (Section 4.2.1). Temperature profiles are analyzed along (a) $x = 0.15$, (b) $x = 0.85$, (c) $y = 0.15$, and (d) $y = 0.85$, illustrating the impact of Richardson numbers on convective patterns within the cavity.

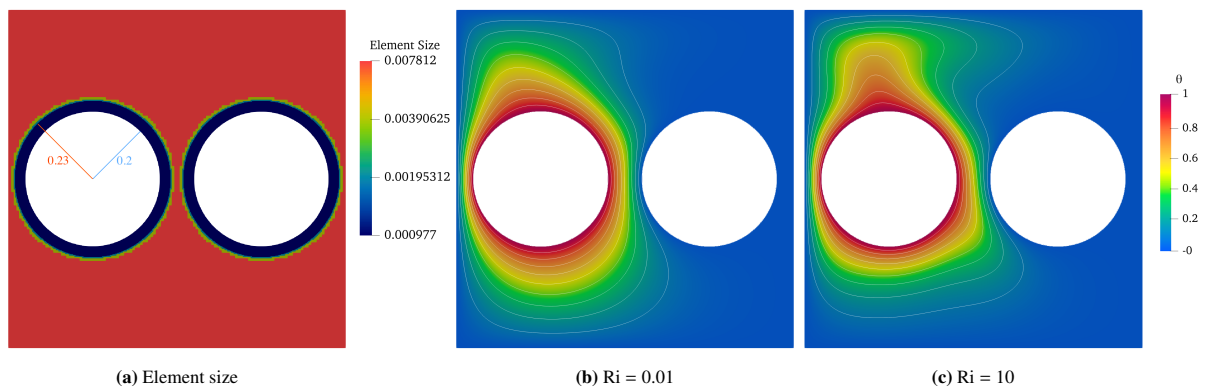


Figure 9: Temperature contours and local mesh refinement are demonstrated in the lid-driven cavity thermal flow case with two circular disks (Section 4.2.1). The contour lines represent non-dimensional temperatures ranging from 0 to 1, plotted at regular intervals of 0.1.

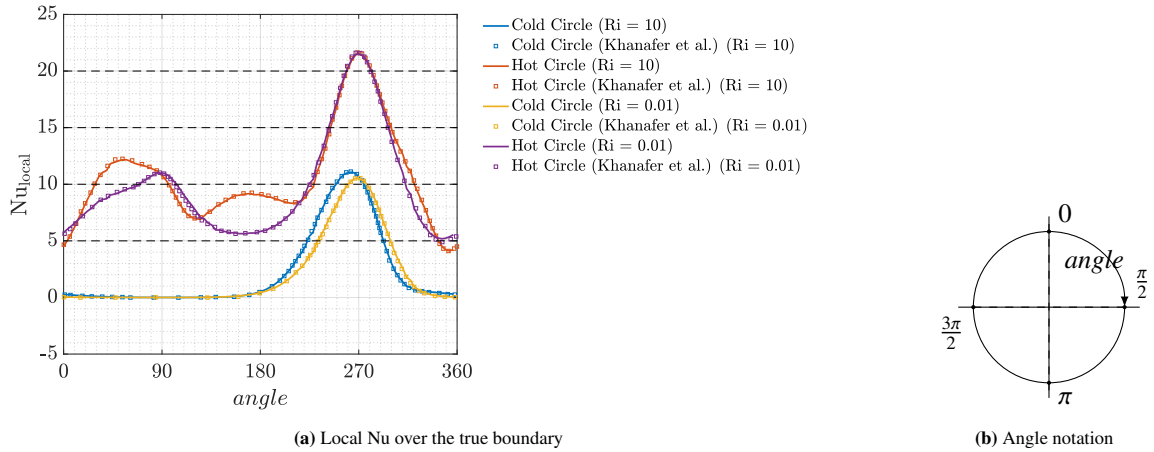


Figure 10: Distribution of the local Nusselt number along the boundary of two circular disks (one cold and one hot) within the lid-driven cavity thermal flow (Section 4.2.1). The simulation results are validated against values from Khanafar et al. [88].

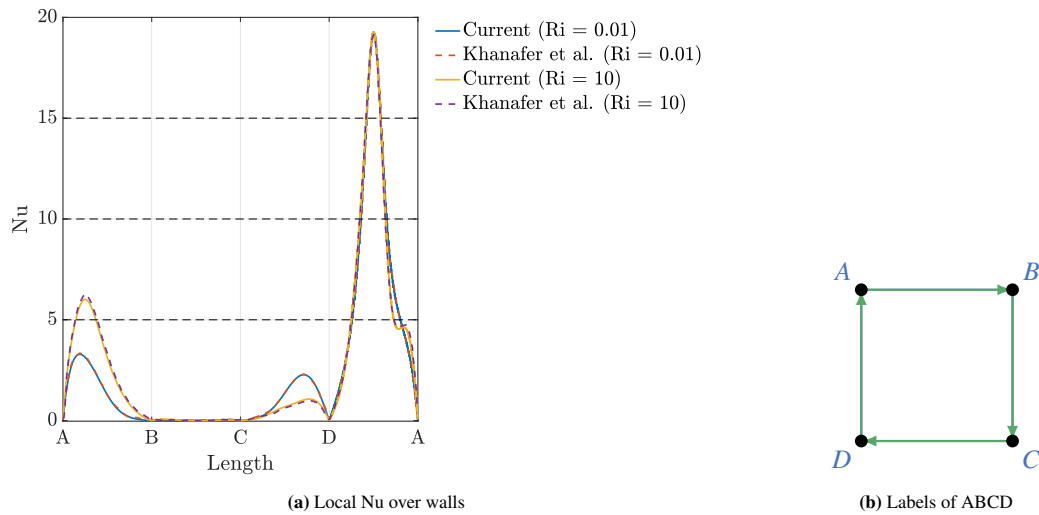


Figure 11: Nusselt number distribution over the four boundary walls of the lid-driven cavity thermal flow with two circular obstacles (Section 4.2.1). Results are benchmarked against the findings of Khanafar et al. [88] for validation and comparison.

4.2.2. Flow past a heated circle with constant wall temperature (CWT)

We next compare our results with several studies on flow past a circular disk with a constant wall temperature (CWT) [89–94]. For these simulations, no-slip and $\theta = 1$ boundary conditions are applied on the boundary of the circular disk using SBM. In addition to the circular disk, the boundary conditions on the domain walls are described in Table 6. The simulations are conducted under forced convection, involving one-way coupling where the heat transfer is influenced by the flow, but the flow remains unaffected by the heat. The simulation domain spans $[0, 50] \times [0, 40]$, with the circular disk positioned at the center (20, 20). Details of the mesh configuration are provided in Table 7. Using this mesh, simulations are performed for Reynolds numbers ranging from 21580 to 50350, demonstrating the effectiveness of our approach to local mesh refinement. Figure 12 depicts the mesh refinement, emphasizing the fine boundary mesh near the circular disk that accurately captures the thermal boundary layer. The simulation results are presented in Figure 13a and summarized in Table 8.

Our investigation achieved consistency between our findings and those reported in the literature, including experimental and numerical studies. This agreement covers a range of Reynolds numbers, from 100 to 50350. Additionally, we computed the local flux on the actual boundary of the circle, achieving a good match with the literature, as shown in Figure 13b, which demonstrates the capability of the SBM to capture the first derivative on the INTERCEPTED elements accurately.

Table 6: Boundary conditions for flow past a circular disk with constant wall temperature (Section 4.2.2).

Boundary	Navier-Stokes (Velocity)	Heat Transfer (Temperature, θ)
Inlet (Left Side)	$u = 1, v = 0$	$\theta = 0$
Outlet (Right Side)	Backflow stabilization	Backflow stabilization for temperature
Top Wall	$u = 1, v = 0$	$\theta = 0$
Bottom Wall	$u = 1, v = 0$	$\theta = 0$

Table 7: Mesh specifications for simulations of flow past a circular disk with constant wall temperature (CWT) across varying Reynolds numbers (Section 4.2.2).

Reynolds Number	100	500	7190	21580	35950	50350
$\frac{\bar{D}}{h}$	2622	2622	10486	20971	20971	20971
Total mesh nodes	1573621	1573621	1849272	2252484	2252484	2252484

Table 8: Comparative Nusselt number values at different Reynolds numbers for flow past a CWT circular disk, benchmarking against various literature sources (Section 4.2.2).

Reynolds Number	100	500	7190	21580	35950	50350
Scholten and Murray [89]			51.00	103.40	127.50	155.10
Szczepanik et al. [90]			67.30	148.00		191.10
Nakamura and Igarashi [91]	6.21	13.19	51.68	102.17		
Zukauskas and Ziugzda [92]	5.10	10.78	47.3	91.30	124.00	151.70
Pachpute et al. [93]	5.18	12.17	55.52	111.45	142.86	171.28
Hsu [94]	5.25	12.28				
Octree-SBM	5.13	11.93	56.40	101.74	132.09	159.29

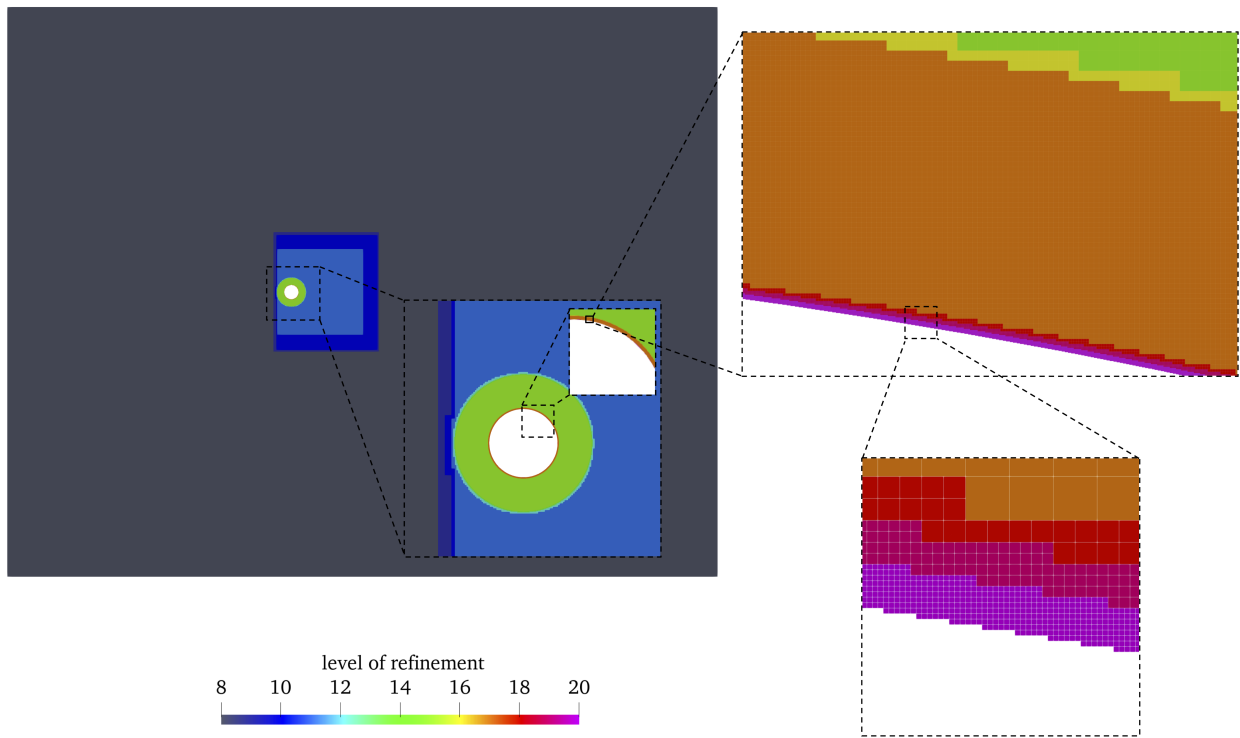
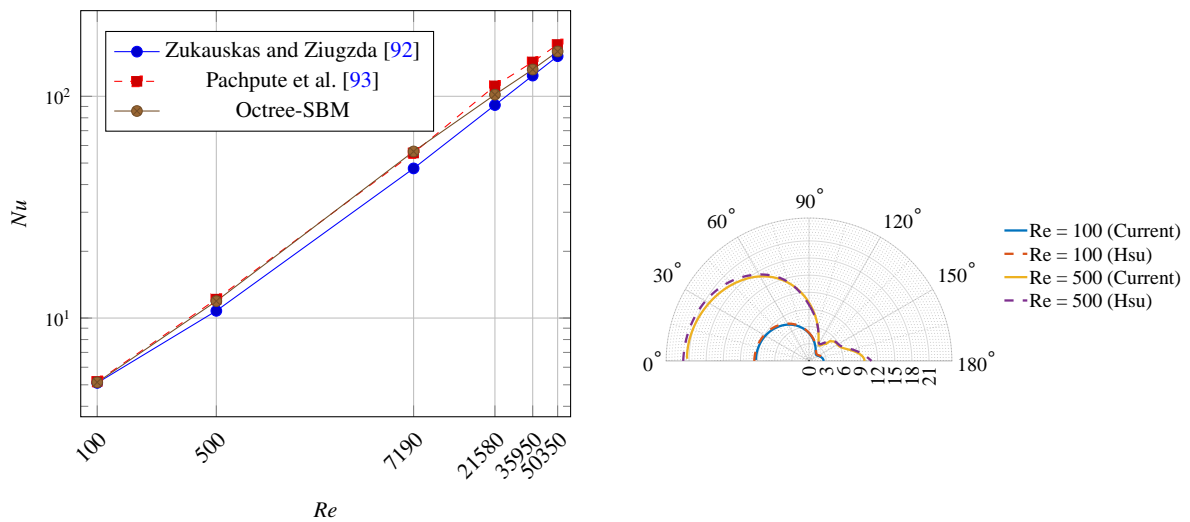


Figure 12: Levels of refinement for flow past a circular disk with constant wall temperature (CWT), highlighting mesh refinement near the disk to resolve the thermal boundary layer (Section 4.2.2).



(a) Relationship between Reynolds number (Re) and Nusselt number (Nu) for flow past a CWT circular disk, comparing results with existing literature. **(b)** Angular distribution of local Nusselt number comparing with Hsu [94] for $Re = 100$ and $Re = 500$ around the boundary of a CWT circular disk.

Figure 13: Comparison of Nusselt numbers across various Reynolds numbers and angular positions for flow past a CWT circular disk (Section 4.2.2).

4.3. Neumann boundary condition for heat transfer in 2D: flow past a circular disk with uniform heat flux (UHF)

In addition to the Dirichlet boundary condition, the Neumann boundary condition, often referred to as a flux boundary condition in the context of convection-diffusion equations, is essential in thermal incompressible flow problems. We first consider a case similar to Section 4.2.2 – a forced convection problem. We put a disk with uniform heat flux (UHF) boundary condition [95–97] on the center of the fluid domain whose domain size is $[0, 61] \times [0, 61]$ based on what is suggested in the literature [97]. We applied velocity boundary conditions of $(1, 0)$ on the top, left, and bottom walls. On the right wall, we prescribed a pressure of zero. For the heat transfer problem, we implemented zero-flux boundary conditions for all walls, with the exception of the left wall, which was set to a fixed temperature of $\theta = 0$. The non-dimensional uniform heat flux applied to the disk, denoted as $q^* = \frac{\partial \theta}{\partial n}$, is assigned a value of -1 . Here, n is directed inwards towards the disk. Consequently, the fluid system experiences an increase in energy due to the introduction of this heat flux. In this simulation, we applied three different levels of mesh refinement. The region closest to the circular disk is refined to level 13 (mesh size = $61 \cdot 2^{-13}$). Surrounding this is a larger rectangular region with a refinement level of 8 (mesh size = $61 \cdot 2^{-8}$). The base refinement level for the entire simulation is 7 (mesh size = $61 \cdot 2^{-7}$). Due to the 2:1 balancing constraint in our octree mesh framework, intermediate refinement levels are automatically introduced between levels 13 and 8. The mesh is shown in Figure 14.

The temperature contour after the flow reach steady state for different Reynolds number are illustrated in Figure 15. Table 9 presents the results obtained by applying the SBM for Neumann boundary conditions with the literature. We conducted experiments to evaluate the impact of the area correction term ($n \cdot \tilde{n}$) by comparing the results with and without its inclusion in Table 10. It is crucial to note that, without including the area correction term ($n \cdot \tilde{n}$), the obtained Nu value on the true boundary deviates from its true value. The SBM plays a vital role in ensuring that the pixelated octree-based mesh satisfies the boundary conditions on the true boundary. Without the application of the area correction term (i.e., by setting $n \cdot \tilde{n} = 1$), the numerical error becomes significant, reaching an order of $O(1)$ shown in Table 10. We can see that the solution without area correction is way off the literature results. $O(1)$ errors imply that the errors persist no matter how much the mesh is refined. This illustrates that the SBM strategy is a viable strategy for imposing Neumann boundary conditions.

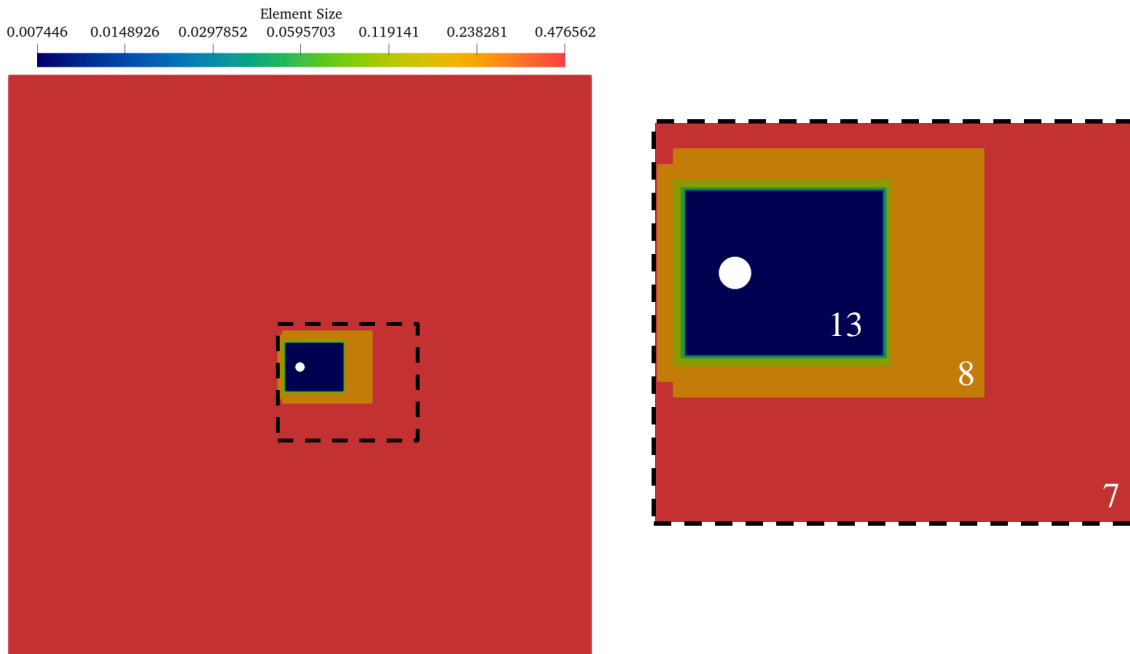


Figure 14: Mesh refinement levels for flow past a circular disk with uniform heat flux (UHF), highlighting finer element sizes near the disk to accurately capture heat transfer effects (Section 4.3).

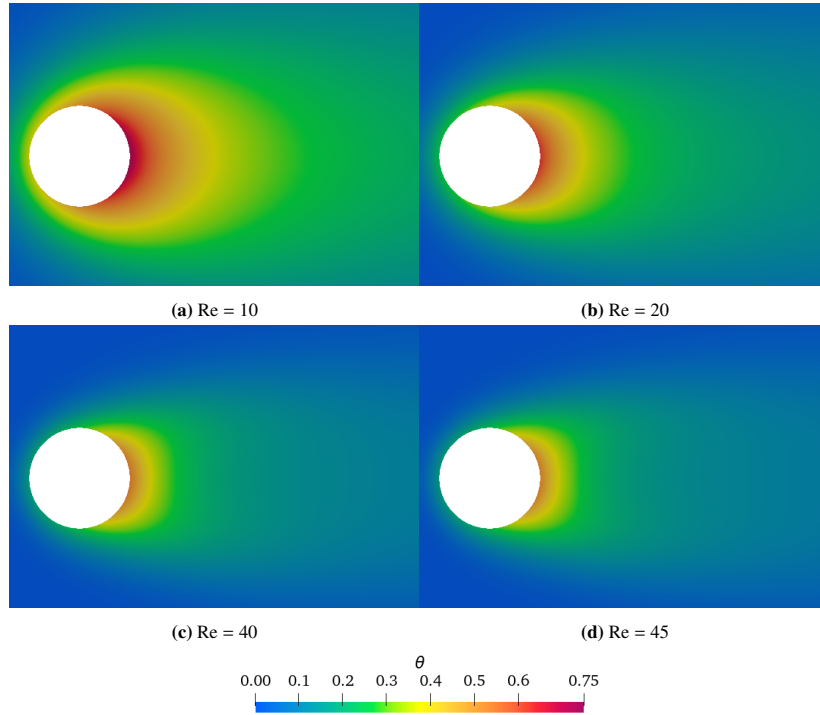


Figure 15: Temperature contours at steady-state for flow past a circular disk with uniform heat flux (UHF) under various Reynolds numbers (Section 4.3).

Table 9: Comparison of Nusselt numbers obtained using the Octree-Shifted Boundary Method (Octree-SBM) with literature values across different Reynolds numbers for flow past a UHF circular disk (Section 4.3).

Study	Re = 10	Re = 20	Re = 40	Re = 45
Bharti et al. [97]	2.0400	2.7788	3.7755	3.9727
Ahmad and Qureshi [96]	2.0410	2.6620	3.4720	-
Dennis et al. [95]	2.1463	2.8630	3.7930	-
Octree-SBM	2.0365	2.7534	3.7640	3.9630

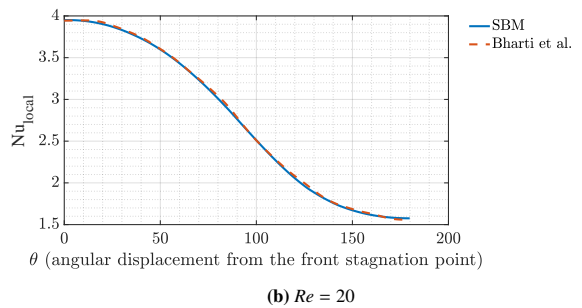
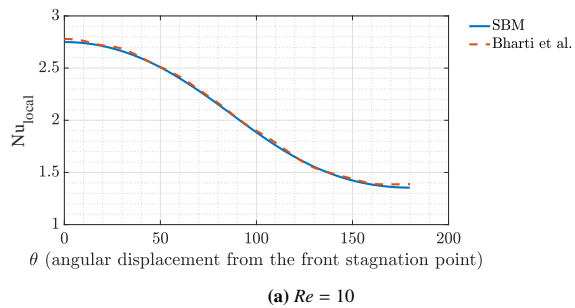


Figure 16: Comparison of the local Nusselt number distribution with Bharti et al. [97] as a function of the angular position around a UHF circular disk for selected Reynolds numbers (Section 4.3).

Table 10: Comparison of Nusselt numbers with and without the area correction term for Neumann boundary conditions, highlighting the importance of the area correction term ($\tilde{n}_j n_j$ in the SBM Neumann term in Eq. 35) for achieving accurate results (Section 4.3).

Re	10	20	40
Area Correction	2.0365	2.7534	3.7640
Without Area Correction (by setting $n \cdot \tilde{n} = 1$)	2.5794	3.5024	4.7362
Bharti et al. [97]	2.0400	2.7788	3.7755

4.4. Natural convection around a 3D sphere in a cubic enclosure

We conduct simulations similar to those presented in [87, 98], where a heated sphere with a radius of 0.2 is placed inside a cold environment bounded by a cube with edge lengths of 1. This setup is used to observe natural convection driven by the temperature difference. The boundary conditions are set as $\theta = 1$ at the surface of the sphere and $\theta = 0$ at the cube's walls. No-slip boundary conditions are applied to all walls and the sphere's boundary. Unlike the mixed convection problem discussed in Section 4.2.1 and the forced convection problems in Section 4.2.2 and Section 4.3, this subsection focuses exclusively on natural convection. We simulate a wide range of Rayleigh numbers ranging from 10^3 all the way to 10^8 .

For $Ra = 10^3$ and 10^4 , a spherical refinement region with a radius of 0.35, centered at the same location as the sphere, is set to level 8 (mesh size = 2^{-8}), while the base refinement level is set to 6 (mesh size = 2^{-6}). Additionally, a cylindrical refinement region with a radius of 0.35 is applied, with its centerline aligned with that of the cube, extending from the bottom wall to the top wall. The mesh sizes for these two cases are shown in Figure 17a. For $Ra = 10^5$ and 10^6 , the spherical refinement region, with a radius of 0.35 and centered at the sphere, remains at level 8 (mesh size = 2^{-8}), but the base refinement level is increased to 7 (mesh size = 2^{-7}). The mesh sizes for these cases are shown in Figure 17b. For $Ra = 10^7$ and 10^8 , the refinement strategy is similar to that for $Ra = 10^5$ and 10^6 , with an additional level 9 refinement (mesh size = 2^{-9}) applied at the boundary of the cube, and an additional spherical refinement region at level 9 with a radius of 0.25, centered at the sphere. The mesh sizes for these cases are shown in Figure 17c.

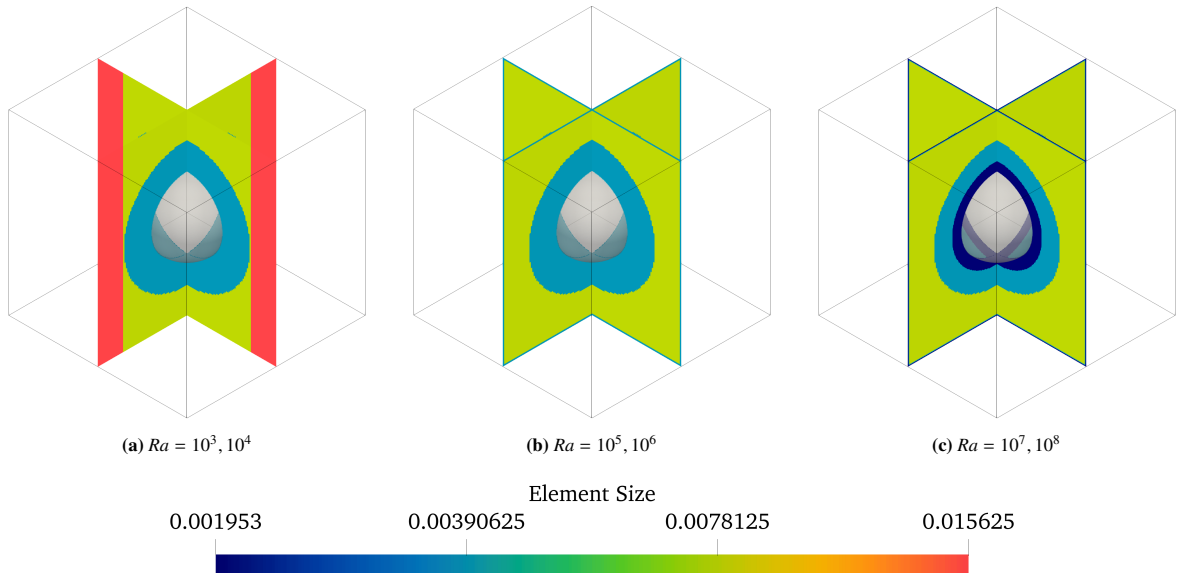


Figure 17: Element size for the natural convection simulation around a 3D sphere within a cubic enclosure, shown for various Rayleigh numbers. (Section 4.4)

Table 11: Mesh convergence study results for natural convection around a 3D sphere in a cubic enclosure, detailing the effect of different element sizes on Nusselt number values. The Nusselt numbers are defined as follows: \overline{Nu}_T represents the average Nusselt number at the top boundary, \overline{Nu}_B at the bottom boundary, \overline{Nu}_S at the side boundaries, and \overline{Nu}_{Sp} on the surface of the sphere (Section 4.4).

Ra	Highest refine level	\overline{Nu}_T	\overline{Nu}_B	\overline{Nu}_S	\overline{Nu}_{Sp}
10^7	7	10.51	0.02	1.27	29.05
	8	11.25	0.02	1.32	31.63
	9	11.57	0.02	1.35	33.05

Table 12: Nusselt number comparisons for natural convection around a heated sphere within a cubic enclosure at varying Rayleigh numbers, benchmarked against literature values (Section 4.4).

Ra	Study	\overline{Nu}_T	\overline{Nu}_B	\overline{Nu}_S	\overline{Nu}_{Sp}
10^3	Yoon et al. [98] (FVM)	0.69	0.62	0.66	7.42
	Chen et al. [87] (LBM)	0.71	0.63	0.67	7.97
	Octree-SBM	0.69	0.61	0.64	7.41
10^4	Yoon et al. [98] (FVM)	1.23	0.38	0.64	7.80
	Chen et al. [87] (LBM)	1.23	0.39	0.66	8.46
	Octree-SBM	1.2	0.37	0.63	7.81
10^5	Yoon et al. [98] (FVM)	3.87	0.08	0.67	12.61
	Chen et al. [87] (LBM)	3.91	0.09	0.69	13.42
	Octree-SBM	3.77	0.09	0.65	12.34
10^6	Yoon et al. [98] (FVM)	6.97	0.04	0.97	20.64
	Chen et al. [87] (LBM)	6.94	0.04	1.02	22.58
	Octree-SBM	6.63	0.04	0.92	19.87
10^7	Octree-SBM	11.57	0.02	1.35	33.05
10^8	Octree-SBM	18.75	0.01	2.23	54.82

Table 13: Comparative drag force coefficients for natural convection around a 3D sphere in a cubic enclosure at different Rayleigh numbers (Section 4.4). Here, the direction of gravity is $-y$.

Ra	\overline{C}_x	\overline{C}_y	\overline{C}_z
10^3	$-3.8 \cdot 10^{-3}$	0.4923	$-9.81 \cdot 10^{-4}$
10^4	$-3.8 \cdot 10^{-3}$	0.5063	$-9.65 \cdot 10^{-4}$
10^5	$-3.86 \cdot 10^{-4}$	0.2160	$-1.84 \cdot 10^{-4}$
10^6	$-1.88 \cdot 10^{-4}$	0.1291	$-8.81 \cdot 10^{-5}$
10^7	$1.57 \cdot 10^{-5}$	0.0351	$1.52 \cdot 10^{-5}$
10^8	$2.7 \cdot 10^{-5}$	0.0182	$4.38 \cdot 10^{-5}$

For $Ra = 10^7$, we conduct a mesh convergence study by testing three different refinements in the spherical refinement region near the sphere and along the cube's boundary, as shown in Table 11. The Nusselt numbers on the walls and the sphere converge to specific values. In Table 12, we list the Nusselt numbers on the walls and the sphere for $Ra = 10^3$ through $Ra = 10^8$. For $Ra = 10^3$ to $Ra = 10^6$, we also include results from the literature for comparison. In Table 13, we list the drag force coefficients acting on the sphere. Specifically, the drag force coefficients are calculated as the ratio of the force to the cross-sectional area ($\pi \times 0.2^2$) associated with that force.

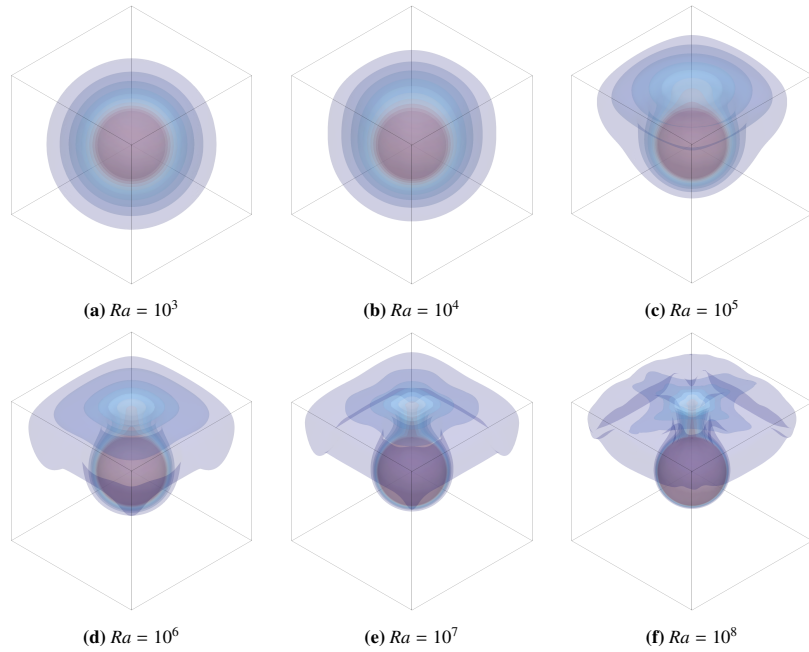


Figure 18: Instantaneous temperature contours for a hot sphere in a cubic enclosure at various Rayleigh numbers, with contours plotted from 0 to 1 in non-dimensional temperature at intervals of 0.1 (Section 4.4).

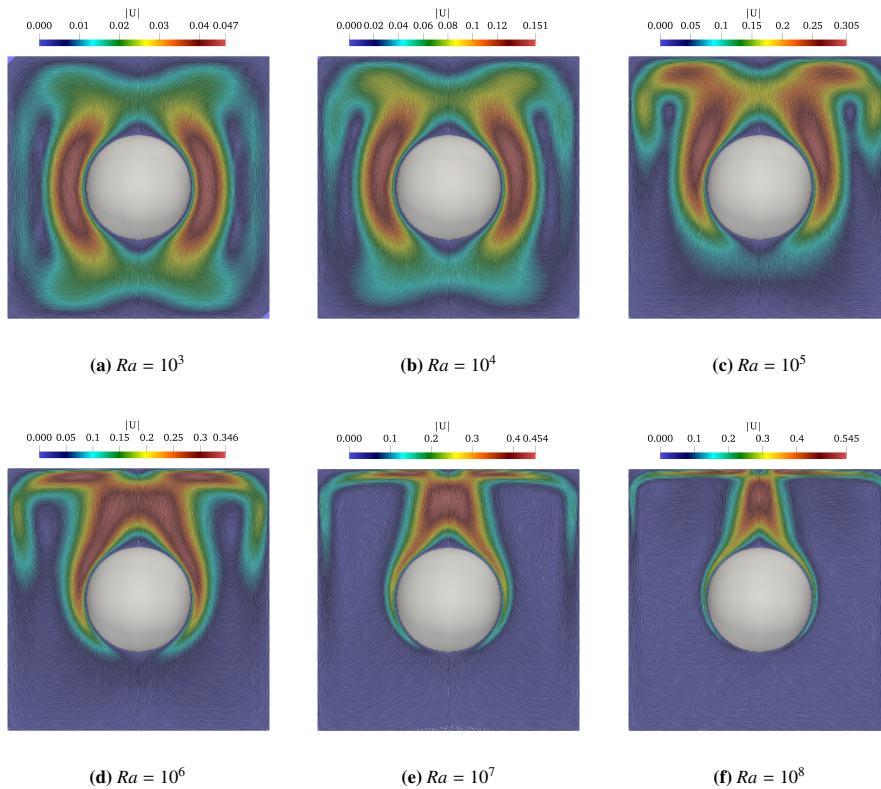
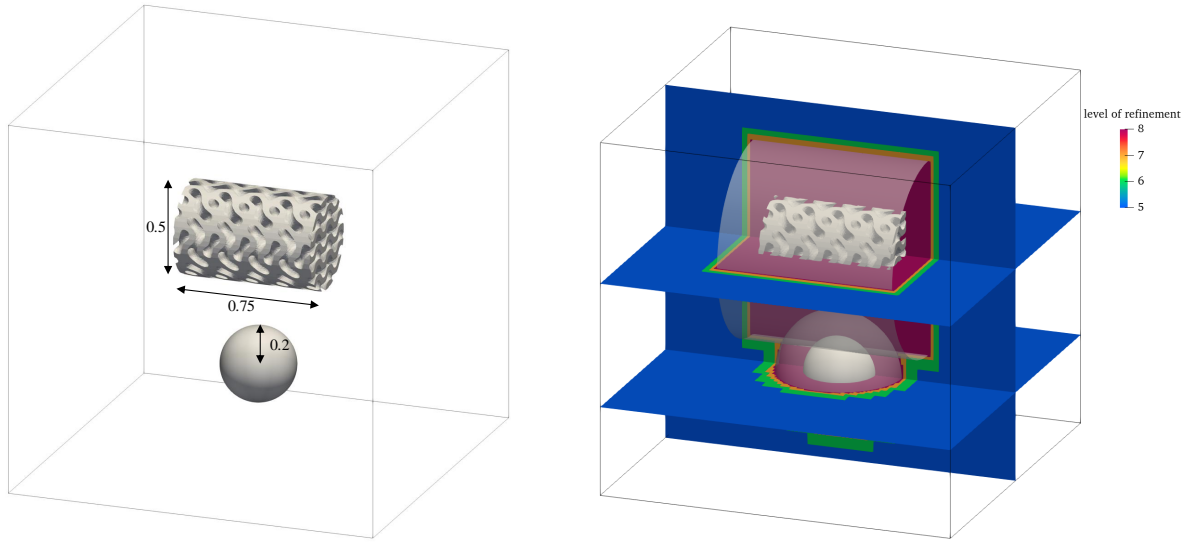


Figure 19: Instantaneous velocity Line Integral Convolution (LIC) visualizations for natural convection around a heated sphere in a cubic enclosure at various Rayleigh numbers (Section 4.4).



(a) Schematic of the problem setup for natural convection around a three-dimensional sphere and a gyroid structure enclosed within a cubic domain.

(b) Refinement levels for the computational mesh, illustrating local mesh refinement in the vicinity of the larger cylindrical region aligned with the gyroid's centerline and the larger spherical region.

Figure 20: Illustration of the problem setup and mesh refinement strategy for natural convection simulations within a cubic enclosure (Section 4.5)

4.5. Natural convection around an 3D sphere and gyroid in a cubic enclosure

We finally illustrate our framework on a case exhibiting a very complex geometry and coupled thermal fluid phenomena. We include a gyroid structure to the previous case, as illustrated in Figure 20. The gyroid exhibits an intricate geometry – which makes creating body fitted meshes very difficult – and enforcing thermal and no-slip conditions in conventional immersed boundary approaches is non-trivial. In our Linearized Octree-SBM approach this geometry and associated boundary conditions are trivially simple to account for.

The boundary conditions applied to the walls of the cube for both the Navier-Stokes and heat transfer equations in this problem are identical with those outlined in Section 4.4. We applied $\theta = 1$ and no-slip on the gyroid, and $\theta = -1$ and no-slip on the sphere. The fluid domain is a larger box with dimensions $[0, 2] \times [0, 2] \times [0, 2]$, containing a sphere with a radius of 0.2 positioned at $(1, 0.5, 1)$ and a gyroid structure with a radius of 0.5 and a lateral length of 0.75, located at $(1, 1.2, 1)$. The mesh refinement strategy includes a base refinement level of 5 (mesh size = $2 \cdot 2^{-5}$). Additional local mesh refinements at a level of 8 (mesh size = $2 \cdot 2^{-8}$) are applied in two regions: (a) a larger cylinder with a radius of 0.55, aligned with the gyroid's centerline, and (b) a larger sphere with a radius of 0.55, centered at the same location as the sphere geometry. The mesh refinement levels around the geometries are illustrated in Figure 20b. We have selected a Rayleigh number of $Ra = 10^3$. Visualizations of the streamlines and temperature contours are shown in Figure 21a and Figure 21b.

The streamlines are colored by the y-direction velocity of the flow, indicating that the heated sphere generates an upward flow with positive y-velocity in the surrounding region. Conversely, the y-direction velocity near the Gyroid is negative due to the cooler temperature, which induces a downward flow. In Figure 21b, the zero-temperature contour closely follows the shape of the Gyroid, demonstrating Octree-SBM's effectiveness in accurately enforcing boundary conditions. These visualizations provide a detailed depiction of the intricate flow behavior induced by the gyroid structure in a natural convection scenario. The front view (Figure 22) captures the directional shifts of the streamlines as they interact with the gyroid, revealing the path of streamlines navigating through the gyroid's lattice-like geometry and emphasizing the complex routes shaped by its porous structure.

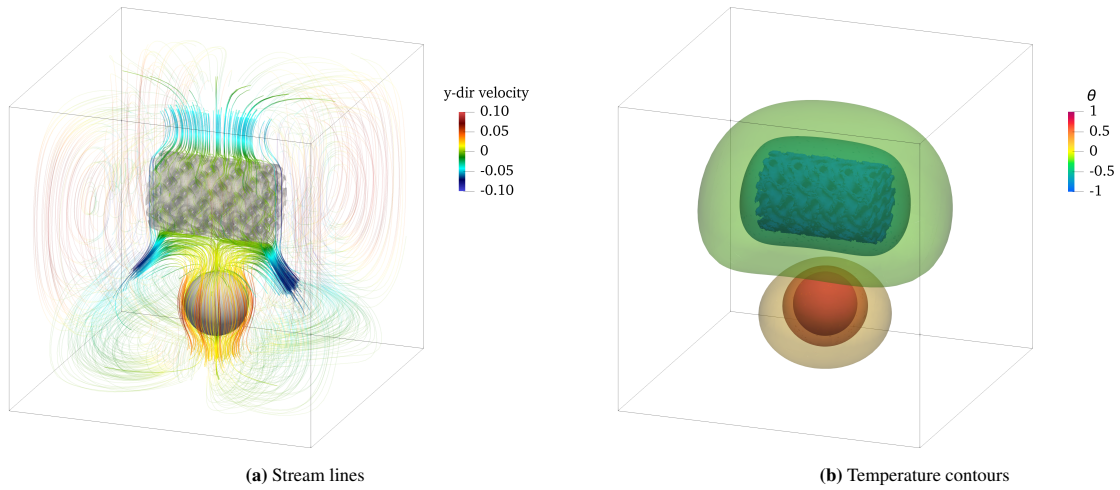


Figure 21: Streamlines and temperature contours for natural convection around a 3D sphere and a Gyroid structure within a cubic enclosure, with contour values set to -1, -0.6, -0.2, 0.2, 0.6, and 1. Streamlines are colored by the y-direction velocity (Section 4.5).

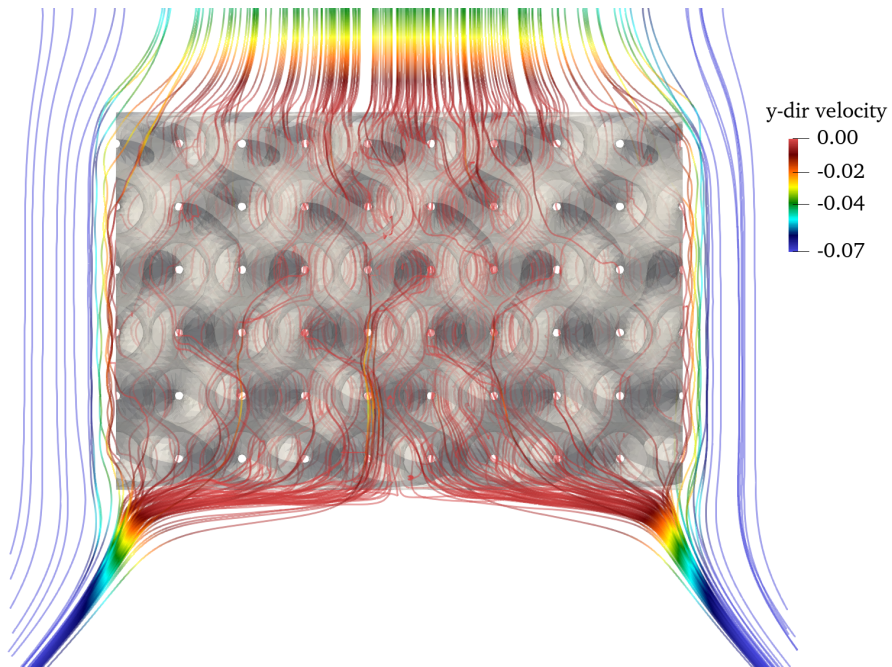


Figure 22: Streamlines passing through a Gyroid (Front view). The image highlights the directional change of streamlines as they navigate through the Gyroid structure within a cubic enclosure, offering a detailed perspective of natural convection patterns (Section 4.5).

4.6. Parallel performance of the Octree-SBM framework: strong scaling test

We present the scaling performance of our framework on the TACC [Frontera](#) system. For this study, we analyze the problem outlined in [Section 4.3](#). The simulations are conducted at a Reynolds number of 40 and a Peclet number of 28, using a computational mesh comprising 548870 nodes. Starting from the initial condition, the simulations advance with a non-dimensional time step of 1 until reaching a total non-dimensional time of 5. A scaling analysis is performed, employing $56 \times n$ processors, where n varies from 1 to 8.

We utilize [PETSc](#) solvers for both the Navier-Stokes (NS) and heat transfer (HT) equations in our simulations. The NS equations are solved using the GMRES (Generalized Minimal Residual) method with a restart value of 1000, coupled with the Additive Schwarz Method (ASM) preconditioner configured with an overlap of 10. Similarly, for the heat transfer (HT) equations, we use the GMRES solver with a restart value of 1000 and an ASM preconditioner configured with an overlap of 3. [Figure 23](#) illustrates the scalability of our approach, demonstrating the progression of total solution time as the processor count increases. The performance closely approximates an idealized scaling pattern, as represented by the reference dashed line in the plot.

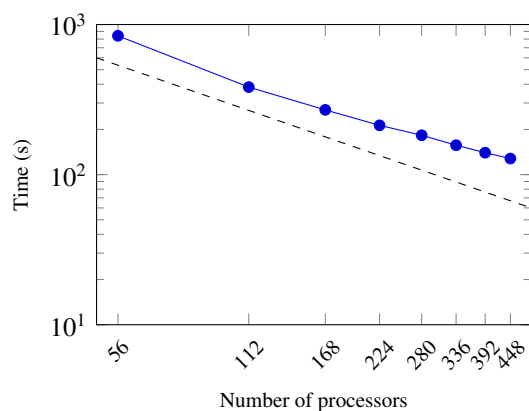


Figure 23: Scaling performance of the Octree-SBM computation for 2D flow past a cylinder with a uniform heat flux, as evaluated on TACC’s [Frontera](#) supercomputer ([Section 4.6](#)).

5. Conclusions and Future Work

The challenges posed by accurately simulating thermal incompressible flows in domains with complex geometries motivate the development of more versatile and efficient computational frameworks. Traditional boundary-fitted methods, though precise, struggle with scalability and preprocessing demands. Addressing these limitations, this study explored the potential of the Shifted Boundary Method (SBM) integrated with an octree-based discretization scheme. This approach aligns with the growing need for adaptable, high-performance tools capable of tackling multiphysics scenarios in diverse flow regimes and geometries.

Key contributions of this work include the application of the SBM for coupled thermal flow simulations using linearized Navier-Stokes and heat transfer equations, which significantly enhance computational efficiency. The use of octree meshes facilitates accurate boundary condition enforcement in complex geometries, while comprehensive validation across 2D and 3D cases demonstrates robustness across laminar, transitional, and turbulent regimes. Furthermore, the framework’s ability to handle Dirichlet and Neumann boundary conditions with high precision underscores its versatility and accuracy, paving the way for applications in a wide array of engineering and scientific domains.

Looking ahead, several exciting avenues for further exploration emerge. Extending the framework to encompass more complex multiphysics problems, such as fluid-structure interaction, could significantly broaden its applicability. Incorporating adaptive mesh refinement (AMR) techniques could enhance both accuracy and computational efficiency, while higher-order finite element basis functions may improve solution fidelity. Additionally, the current linearized approach, though efficient, may require enhancements to address highly nonlinear flow regimes effectively. Addressing these challenges will further solidify the Octree-SBM’s role as a powerful tool in the computational modeling of thermal flows.

References

- [1] M. M. A. Bhutta, N. Hayat, M. H. Bashir, A. R. Khan, K. N. Ahmad, S. Khan, CFD applications in various heat exchangers design: A review, *Applied Thermal Engineering* 32 (2012) 1–12.
- [2] C. Abeykoon, Compact heat exchangers–design and optimization with CFD, *International Journal of Heat and Mass Transfer* 146 (2020) 118766.
- [3] R. Priyadarsini, W. N. Hien, C. K. W. David, Microclimatic modeling of the urban thermal environment of singapore to mitigate urban heat island, *Solar energy* 82 (2008) 727–745.
- [4] J. Allegrini, J. Carmeliet, Simulations of local heat islands in zürich with coupled CFD and building energy models, *Urban climate* 24 (2018) 340–359.
- [5] B. Chenari, J. D. Carrilho, M. G. Da Silva, Towards sustainable, energy-efficient and healthy ventilation strategies in buildings: A review, *Renewable and Sustainable Energy Reviews* 59 (2016) 1426–1447.
- [6] H. Zhang, D. Yang, V. W. Tam, Y. Tao, G. Zhang, S. Setunge, L. Shi, A critical review of combined natural ventilation techniques in sustainable buildings, *Renewable and Sustainable Energy Reviews* 141 (2021) 110795.
- [7] S. Bhattacharyya, K. Dey, A. R. Paul, R. Biswas, A novel CFD analysis to minimize the spread of COVID-19 virus in hospital isolation room, *Chaos, Solitons & Fractals* 139 (2020) 110294.
- [8] Y. Li, H. Qian, J. Hang, X. Chen, P. Cheng, H. Ling, S. Wang, P. Liang, J. Li, S. Xiao, et al., Probable airborne transmission of sars-cov-2 in a poorly ventilated restaurant, *Building and environment* 196 (2021) 107788.
- [9] A. Foster, M. Kinzel, Estimating covid-19 exposure in a classroom setting: A comparison between mathematical and numerical models, *Physics of Fluids* 33 (2021).
- [10] K. Saurabh, M. Ishii, M. Fernando, B. Gao, K. Tan, M.-C. Hsu, A. Krishnamurthy, H. Sundar, B. Ganapathysubramanian, Scalable adaptive pde solvers in arbitrary domains, in: *Proceedings of the International Conference for High Performance Computing, Networking, Storage and Analysis*, 2021, pp. 1–15.
- [11] K. Tan, B. Gao, C.-H. Yang, E. L. Johnson, M.-C. Hsu, A. Passalacqua, A. Krishnamurthy, B. Ganapathysubramanian, A computational framework for transmission risk assessment of aerosolized particles in classrooms, *Engineering with Computers* (2023) 1–22.
- [12] S. Rayegan, C. Shu, J. Berquist, J. Jeon, L. G. Zhou, L. L. Wang, H. Mbareche, P. Tardif, H. Ge, A review on indoor airborne transmission of covid-19–modelling and mitigation approaches, *Journal of Building Engineering* 64 (2023) 105599.
- [13] R. Tali, A. Rabeh, C.-H. Yang, M. Shadkhan, S. Karki, A. Upadhyaya, S. Dhakshinamoorthy, M. Saadati, S. Sarkar, A. Krishnamurthy, et al., Flowbench: A large scale benchmark for flow simulation over complex geometries, *arXiv preprint arXiv:2409.18032* (2024).
- [14] C. S. Peskin, Flow patterns around heart valves: a numerical method, *Journal of Computational Physics* 10 (1972) 252–271.
- [15] R. Mittal, G. Iaccarino, Immersed boundary methods, *Annual Review of Fluid Mechanics* 37 (2005) 239–261.
- [16] T. Colonius, K. Taira, A fast immersed boundary method using a nullspace approach and multi-domain far-field boundary conditions, *Computer Methods in Applied Mechanics and Engineering* 197 (2008) 2131–2146.
- [17] X. Wang, W. K. Liu, Extended immersed boundary method using FEM and RKPM, *Computer Methods in Applied Mechanics and Engineering* 193 (2004) 1305–1321.
- [18] L. Zhang, A. Gerstenberger, X. Wang, W. K. Liu, Immersed finite element method, *Computer Methods in Applied Mechanics and Engineering* 193 (2004) 2051–2067.
- [19] I. Borazjani, L. Ge, F. Sotiropoulos, Curvilinear immersed boundary method for simulating fluid structure interaction with complex 3d rigid bodies, *Journal of Computational physics* 227 (2008) 7587–7620.
- [20] Z. Zhao, J. Yan, Enriched immersed boundary method (eibm) for interface-coupled multi-physics and applications to convective conjugate heat transfer, *Computer Methods in Applied Mechanics and Engineering* 401 (2022) 115667.
- [21] J. Parvizian, A. Düster, E. Rank, Finite cell method: h - and p - extension for embedded domain methods in solid mechanics, *Computational Mechanics* 41 (2007) 122–133.
- [22] A. Düster, J. Parvizian, Z. Yang, E. Rank, The finite cell method for three-dimensional problems of solid mechanics, *Computer Methods in Applied Mechanics and Engineering* 197 (2008) 3768–3782.
- [23] D. Schillinger, Q. Cai, R.-P. Mundani, E. Rank, A review of the finite cell method for nonlinear structural analysis of complex cad and image-based geometric models, in: *Advanced Computing*, Springer, 2013, pp. 1–23.
- [24] A. Stavrev, L. H. Nguyen, R. Shen, V. Varduhn, M. Behr, S. Elgeti, D. Schillinger, Geometrically accurate, efficient, and flexible quadrature techniques for the tetrahedral finite cell method, *Computer Methods in Applied Mechanics and Engineering* 310 (2016) 646–673.
- [25] F. de Prenter, C. V. Verhoosel, G. J. van Zwieten, E. H. van Brummelen, Condition number analysis and preconditioning of the finite cell method, *Computer Methods in Applied Mechanics and Engineering* 316 (2017) 297–327.
- [26] J. Jomo, O. Oztoprak, F. de Prenter, N. Zander, S. Kollmannsberger, E. Rank, Hierarchical multigrid approaches for the finite cell method on uniform and multi-level hp-refined grids, *Computer Methods in Applied Mechanics and Engineering* 386 (2021) 114075.
- [27] D. Kamensky, M.-C. Hsu, D. Schillinger, J. A. Evans, A. Aggarwal, Y. Bazilevs, M. S. Sacks, T. J. R. Hughes, An immersogeometric variational framework for fluid–structure interaction: Application to bioprosthetic heart valves, *Computer Methods in Applied Mechanics and Engineering* 284 (2015) 1005–1053.
- [28] F. Xu, D. Schillinger, D. Kamensky, V. Varduhn, C. Wang, M.-C. Hsu, The tetrahedral finite cell method for fluids: Immersogeometric analysis of turbulent flow around complex geometries, *Computers & Fluids* 141 (2016) 135–154.
- [29] C. Wang, F. Xu, M.-C. Hsu, A. Krishnamurthy, Rapid b-rep model preprocessing for immersogeometric analysis using analytic surfaces, *Computer aided geometric design* 52 (2017) 190–204.
- [30] T. Hoang, C. V. Verhoosel, C.-Z. Qin, F. Auricchio, A. Reali, E. H. van Brummelen, Skeleton-stabilized immersogeometric analysis for incompressible viscous flow problems, *Computer Methods in Applied Mechanics and Engineering* 344 (2019) 421–450.
- [31] F. de Prenter, C. Verhoosel, E. van Brummelen, Preconditioning immersed isogeometric finite element methods with application to flow problems, *Computer Methods in Applied Mechanics and Engineering* 348 (2019) 604–631.

- [32] Q. Zhu, F. Xu, S. Xu, M.-C. Hsu, J. Yan, An immersogeometric formulation for free-surface flows with application to marine engineering problems, *Computer Methods in Applied Mechanics and Engineering* 361 (2019) 112748.
- [33] F. Xu, E. L. Johnson, C. Wang, A. Jafari, C.-H. Yang, M. S. Sacks, A. Krishnamurthy, M.-C. Hsu, Computational investigation of left ventricular hemodynamics following bioprosthetic aortic and mitral valve replacement, *Mechanics Research Communications* 112 (2021) 103604.
- [34] S. Xu, F. Xu, A. Kommajosula, M.-C. Hsu, B. Ganapathysubramanian, Immersogeometric analysis of moving objects in incompressible flows, *Computers & Fluids* 189 (2019) 24–33.
- [35] D. Kamensky, Open-source immersogeometric analysis of fluid–structure interaction using fenics and tigar, *Computers & Mathematics with Applications* 81 (2021) 634–648.
- [36] M. Jaiswal, A. M. Corpuz, M.-C. Hsu, Mesh-driven resampling and regularization for robust point cloud-based flow analysis directly on scanned objects, *Computer Methods in Applied Mechanics and Engineering* 432 (2024) 117426.
- [37] A. Main, G. Scovazzi, The shifted boundary method for embedded domain computations. part i: Poisson and stokes problems, *Journal of Computational Physics* 372 (2018) 972–995.
- [38] A. Main, G. Scovazzi, The shifted boundary method for embedded domain computations. part ii: Linear advection-diffusion and incompressible navier-stokes equations, *J. Comput. Phys.* 372 (2018) 996–1026.
- [39] E. N. Karatzas, G. Stabile, L. Nouveau, G. Scovazzi, G. Rozza, A reduced-order shifted boundary method for parametrized incompressible navier-stokes equations, *Computer Methods in Applied Mechanics and Engineering* 370 (2020) 113273.
- [40] N. M. Atallah, C. Canuto, G. Scovazzi, The second-generation shifted boundary method and its numerical analysis, *Computer Methods in Applied Mechanics and Engineering* 372 (2020) 113341.
- [41] N. Atallah, C. Canuto, G. Scovazzi, The shifted boundary method for solid mechanics, *International Journal for Numerical Methods in Engineering* 122 (2021) 5935–5970.
- [42] N. Atallah, C. Canuto, G. Scovazzi, Analysis of the Shifted Boundary Method for the Poisson problem in domains with corners, *Mathematics of Computation* 90 (2021) 2041–2069.
- [43] O. Colomé, A. Main, L. Nouveau, G. Scovazzi, A weighted shifted boundary method for free surface flow problems, *Journal of Computational Physics* 424 (2021) 109837.
- [44] N. M. Atallah, C. Canuto, G. Scovazzi, The high-order shifted boundary method and its analysis, *Computer Methods in Applied Mechanics and Engineering* 394 (2022) 114885.
- [45] X. Zeng, G. Stabile, E. N. Karatzas, G. Scovazzi, G. Rozza, Embedded domain reduced basis models for the shallow water hyperbolic equations with the shifted boundary method, *Computer Methods in Applied Mechanics and Engineering* 398 (2022) 115143.
- [46] E. Heisler, C.-H. Yang, A. Deshmukh, B. Ganapathysubramanian, H. Sundar, Generating finite element codes combining adaptive octrees with complex geometries, *arXiv preprint arXiv:2305.19398* (2023).
- [47] C.-H. Yang, K. Saurabh, G. Scovazzi, C. Canuto, A. Krishnamurthy, B. Ganapathysubramanian, Optimal surrogate boundary selection and scalability studies for the shifted boundary method on octree meshes, *Computer Methods in Applied Mechanics and Engineering* 419 (2024) 116686.
- [48] A. Main, G. Scovazzi, The shifted boundary method for embedded domain computations. part II: linear advection-diffusion and incompressible navier-stokes equations, *J. Comput. Phys.* 372 (2018) 996–1026.
- [49] O. Colomé, A. Main, L. Nouveau, G. Scovazzi, A weighted shifted boundary method for free surface flow problems, *Journal of Computational Physics* 424 (2021).
- [50] D. Xu, O. Colomé, A. Main, K. Li, N. M. Atallah, N. Abboud, G. Scovazzi, A weighted shifted boundary method for immersed moving boundary simulations of stokes’ flow, *Journal of Computational Physics* 510 (2024) 113095.
- [51] S. Popinet, Gerris: a tree-based adaptive solver for the incompressible euler equations in complex geometries, *Journal of computational physics* 190 (2003) 572–600.
- [52] F. Losasso, F. Gibou, R. Fedkiw, Simulating water and smoke with an octree data structure, in: *Acm siggraph 2004 papers*, 2004, pp. 457–462.
- [53] H. Chen, C. Min, F. Gibou, A numerical scheme for the stefan problem on adaptive cartesian grids with supralinear convergence rate, *Journal of Computational Physics* 228 (2009) 5803–5818.
- [54] M. Theillard, L. F. Djodom, J.-L. Vié, F. Gibou, A second-order sharp numerical method for solving the linear elasticity equations on irregular domains and adaptive grids—application to shape optimization, *Journal of Computational Physics* 233 (2013) 430–448.
- [55] J. Papac, A. Helgadottir, C. Ratsch, F. Gibou, A level set approach for diffusion and stefan-type problems with robin boundary conditions on quadtree/octree adaptive cartesian grids, *Journal of Computational Physics* 233 (2013) 241–261.
- [56] A. Guittet, M. Theillard, F. Gibou, A stable projection method for the incompressible Navier–Stokes equations on arbitrary geometries and adaptive quad/octrees, *Journal of computational physics* 292 (2015) 215–238.
- [57] F. S. Sousa, C. F. Lages, J. L. Ansoni, A. Castelo, A. Simao, A finite difference method with meshless interpolation for incompressible flows in non-graded tree-based grids, *Journal of Computational physics* 396 (2019) 848–866.
- [58] R. Egan, A. Guittet, F. Temprano-Coleto, T. Isaac, F. J. Peaudecerf, J. R. Landel, P. Luzzatto-Fegiz, C. Burstedde, F. Gibou, Direct numerical simulation of incompressible flows on parallel octree grids, *Journal of Computational Physics* 428 (2021) 110084.
- [59] K. Saurabh, B. Gao, M. Fernando, S. Xu, M. A. Khanwale, B. Khara, M.-C. Hsu, A. Krishnamurthy, H. Sundar, B. Ganapathysubramanian, Industrial scale large eddy simulations with adaptive octree meshes using immersogeometric analysis, *Computers & Mathematics with Applications* 97 (2021) 28–44.
- [60] E. Bayat, R. Egan, D. Bochkov, A. Sauret, F. Gibou, A sharp numerical method for the simulation of stefan problems with convective effects, *Journal of Computational Physics* 471 (2022) 111627.
- [61] J. A. van Hooft, S. Popinet, A fourth-order accurate adaptive solver for incompressible flow problems, *Journal of Computational Physics* 462 (2022) 111251.
- [62] K. Yu, B. Dorschner, T. Colonius, Multi-resolution lattice green’s function method for incompressible flows, *Journal of Computational Physics* 459 (2022) 110845.

- [63] J. Kim, C. Min, B. Lee, A super-convergence analysis of the poisson solver with octree grids and irregular domains, *Journal of Computational Physics* 488 (2023) 112212.
- [64] M. Blomquist, S. R. West, A. L. Binswanger, M. Theillard, Stable nodal projection method on octree grids, *Journal of Computational Physics* 499 (2024) 112695.
- [65] C.-H. Yang, G. Scovazzi, A. Krishnamurthy, B. Ganapathysubramanian, Simulating incompressible flows over complex geometries using the shifted boundary method with incomplete adaptive octree meshes, arXiv preprint arXiv:2411.00272 (2024).
- [66] A. N. Brooks, T. J. Hughes, Streamline upwind/ Petrov-galerkin formulations for convection dominated flows with particular emphasis on the incompressible Navier-Stokes equations, *Computer methods in applied mechanics and engineering* 32 (1982) 199–259.
- [67] M. Esmaily Moghadam, Y. Bazilevs, T.-Y. Hsia, I. Vignon-Clementel, A. Marsden, M. (MOCHA, A comparison of outlet boundary treatments for prevention of backflow divergence with relevance to blood flow simulations, *Computational Mechanics* 48 (2011) 277–291. doi:10.1007/s00466-011-0599-0.
- [68] M. Braack, P. B. Mucha, Directional do-nothing condition for the Navier-Stokes equations, *Journal of Computational Mathematics* 32 (2014) 507–521. URL: <http://www.jstor.org/stable/43693956>.
- [69] M. Ishii, M. Fernando, K. Saurabh, B. Khara, B. Ganapathysubramanian, H. Sundar, Solving PDEs in space-time: 4D tree-based adaptivity, mesh-free and matrix-free approaches, in: *Proceedings of the International Conference for High Performance Computing, Networking, Storage and Analysis*, 2019, pp. 1–61.
- [70] M. A. Khanwale, K. Saurabh, M. Ishii, H. Sundar, J. A. Rossmann, B. Ganapathysubramanian, A projection-based, semi-implicit time-stepping approach for the Cahn-Hilliard Navier-Stokes equations on adaptive octree meshes, *Journal of Computational Physics* 475 (2023) 111874.
- [71] S. Kim, K. Saurabh, M. A. Khanwale, A. Mani, R. K. Anand, B. Ganapathysubramanian, Direct numerical simulation of electrokinetic transport phenomena in fluids: Variational multi-scale stabilization and octree-based mesh refinement, *Journal of Computational Physics* 500 (2024) 112747.
- [72] E. Haines, Point in polygon strategies., *Graphics Gems* 4 (1994) 24–46.
- [73] H. Sundar, R. S. Sampath, G. Biros, Bottom-up construction and 2: 1 balance refinement of linear octrees in parallel, *SIAM Journal on Scientific Computing* 30 (2008) 2675–2708.
- [74] M. Fernando, D. Duplyakin, H. Sundar, Machine and application aware partitioning for adaptive mesh refinement applications, in: *Proceedings of the 26th International Symposium on High-Performance Parallel and Distributed Computing*, 2017, pp. 231–242.
- [75] J. L. Blanco, P. K. Rai, nanoflann: a C++ header-only fork of FLANN, a library for nearest neighbor (NN) with kd-trees, <https://github.com/jlblancoc/nanoflann>, 2014.
- [76] T. E. Tezduyar, S. Sathe, R. Keedy, K. Stein, Space-time finite element techniques for computation of fluid-structure interactions, *Computer methods in applied mechanics and engineering* 195 (2006) 2002–2027.
- [77] S. Xu, B. Gao, M.-C. Hsu, B. Ganapathysubramanian, A residual-based variational multiscale method with weak imposition of boundary conditions for buoyancy-driven flows, *Computer Methods in Applied Mechanics and Engineering* 352 (2019) 345–368.
- [78] M. A. Khanwale, A. D. Lofquist, H. Sundar, J. A. Rossmann, B. Ganapathysubramanian, Simulating two-phase flows with thermodynamically consistent energy stable Cahn-Hilliard Navier-Stokes equations on parallel adaptive octree based meshes, *Journal of Computational Physics* (2020) 109674.
- [79] S. Xu, Q. Zhu, M. Fernando, H. Sundar, A finite element level set method based on adaptive octree meshes for thermal free-surface flows, *International Journal for Numerical Methods in Engineering* 123 (2022) 5500–5516.
- [80] C. Liu, X. Zheng, C. Sung, Preconditioned multigrid methods for unsteady incompressible flows, *Journal of Computational physics* 139 (1998) 35–57.
- [81] O. Posdziech, R. Grundmann, A systematic approach to the numerical calculation of fundamental quantities of the two-dimensional flow over a circular cylinder, *Journal of fluids and structures* 23 (2007) 479–499.
- [82] J. Wu, C. Shu, Implicit velocity correction-based immersed boundary-lattice Boltzmann method and its applications, *Journal of Computational Physics* 228 (2009) 1963–1979.
- [83] X. Yang, X. Zhang, Z. Li, G.-W. He, A smoothing technique for discrete delta functions with application to immersed boundary method in moving boundary simulations, *Journal of Computational Physics* 228 (2009) 7821–7836.
- [84] B. Rajani, A. Kandasamy, S. Majumdar, Numerical simulation of laminar flow past a circular cylinder, *Applied Mathematical Modelling* 33 (2009) 1228–1247.
- [85] D. Kamensky, M.-C. Hsu, D. Schillinger, J. A. Evans, A. Aggarwal, Y. Bazilevs, M. S. Sacks, T. J. R. Hughes, An immersed geometric variational framework for fluid-structure interaction: Application to bioprosthetic heart valves, *Computer Methods in Applied Mechanics and Engineering* 284 (2015) 1005–1053.
- [86] A. Main, G. Scovazzi, The shifted boundary method for embedded domain computations. Part II: Linear advection-diffusion and incompressible Navier-Stokes equations, *Journal of Computational Physics* 372 (2018) 996–1026.
- [87] Z. Chen, C. Shu, L. Yang, X. Zhao, N. Liu, Immersed boundary-simplified thermal lattice Boltzmann method for incompressible thermal flows, *Physics of Fluids* 32 (2020). doi:10.1063/1.5138711.
- [88] K. Khanafer, S. Aithal, M. El Haj Assad, I. Pop, Flow and heat transfer in a driven cavity with two cylinders, *Journal of Thermophysics and Heat Transfer* 31 (2015). doi:10.2514/1.T4744.
- [89] J. Scholten, D. Murray, Unsteady heat transfer and velocity of a cylinder in cross flow—i. low freestream turbulence, *International journal of heat and mass transfer* 41 (1998) 1139–1148.
- [90] K. Szczepanik, A. Ooi, L. Aye, G. Rosengarten, A numerical study of heat transfer from a cylinder in cross flow, in: *15th Australasian Fluid Mechanics Conference*, 2004, pp. 13–17.
- [91] H. Nakamura, T. Igarashi, Variation of nusselt number with flow regimes behind a circular cylinder for Reynolds numbers from 70 to 30 000, *International journal of heat and mass transfer* 47 (2004) 5169–5173.
- [92] A. Zukauskas, J. Ziugzda, *Heat transfer of a cylinder in crossflow*, Hemisphere Publishing, 1985.
- [93] S. Pachpute, B. Premachandran, P. Talukdar, A numerical study of combined forced convection and gas radiation from a circular cylinder in

- cross flow, *Heat Transfer Engineering* 36 (2015) 135–151.
- [94] L.-C. Hsu, Heat transfer of flow past a cylinder with a slit, *International Journal of Thermal Sciences* 159 (2021) 106582.
- [95] S. C. R. Dennis, J. Hudson, N. Smith, Steady laminar forced convection from a circular cylinder at low Reynolds numbers, *The Physics of Fluids* 11 (1968) 933–940.
- [96] R. Ahmad, Z. Qureshi, Laminar mixed convection from a uniform heat flux horizontal cylinder in a crossflow, *Journal of Thermophysics and Heat Transfer* 6 (1992) 277–287.
- [97] R. P. Bharti, R. Chhabra, V. Eswaran, A numerical study of the steady forced convection heat transfer from an unconfined circular cylinder, *Heat and Mass Transfer* 43 (2007) 639–648.
- [98] H. Yoon, D. Yu, M. Ha, Y. Park, Three-dimensional natural convection in an enclosure with a sphere at different vertical locations, *International Journal of Heat and Mass Transfer* 53 (2010) 3143–3155.

Appendix A. Validation of simulation code

Appendix A.1. 2D manufactured solutions for linearized Navier Stokes

To assess the convergence behavior of the linearized Navier-Stokes on Octree-SBM, we apply the technique of manufactured solutions. This approach involves selecting a solenoidal solution and substituting it into the Navier-Stokes equations. The resulting residual is then treated as a forcing term on the right-hand side. For our analysis, the manufactured solutions along with their corresponding forcing terms are defined as follows:

$$\begin{aligned}\vec{v} &= (\pi \sin^2(\pi x) \sin(2\pi y) \sin(t), -\pi \sin(2\pi x) \sin^2(\pi y) \sin(t)), \\ p &= \cos(\pi x) \sin(\pi y) \sin(t).\end{aligned}\tag{A.1}$$

The spatial convergence plot with constant timestep k are shown in [Figure A.1a](#).

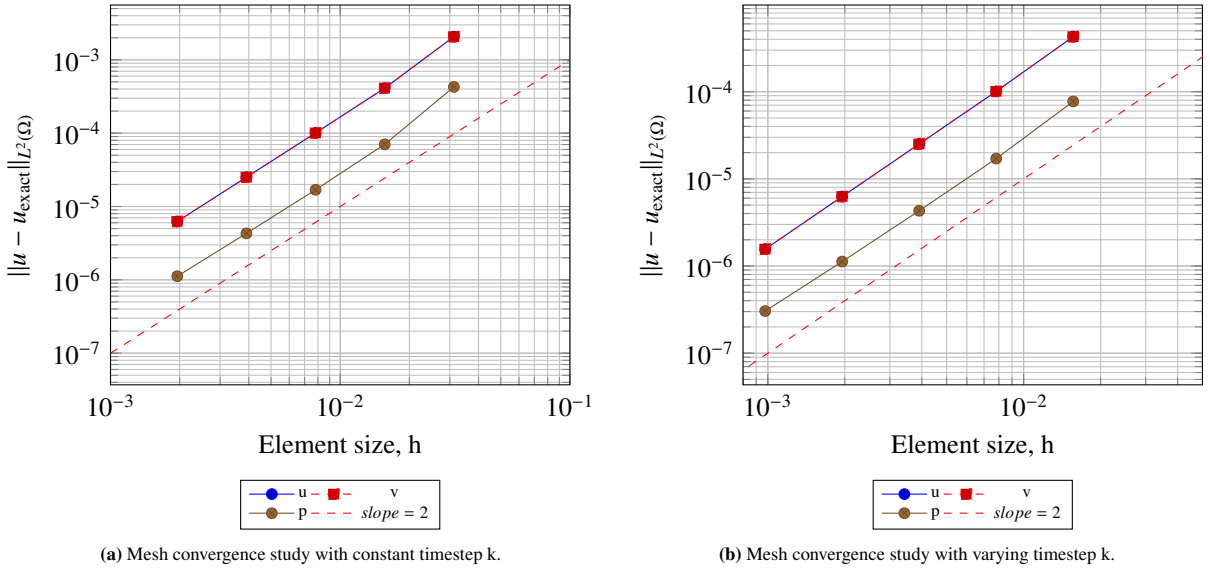


Figure A.1: Mesh convergence results (spatial convergence).

In addition to testing the case with a constant timestep k , we have also evaluated the method of manufactured solutions (MMS) using a continuously varying timestep, based on the BDF2 coefficients shown in [Table 1](#). Specifically, we implemented a linear increase in the timestep from $\frac{k}{4}$ to k , followed by a linear decrease from k back to $\frac{k}{4}$, as illustrated in [Figure A.2](#) with $k = 0.157$. The spatial convergence results for varying k are shown in [Figure A.1b](#). The results of the MMS temporal convergence are presented in [Figure A.3](#). As expected, the correct choice of coefficients produces the theoretical second order convergence in time behavior.

Appendix A.2. Rayleigh-Bénard convection problem

For the Rayleigh-Bénard convection problem (RB problem) with the boundary conditions showing in [Figure A.4](#), we run with two different Ra values: 10^5 and 10^9 with our linearized Navier-Stokes framework. The temperature and velocity fields with LIC for $Ra = 10^5$ and $Ra = 10^9$ are shown in [Figure A.5](#). For $Ra = 10^5$, we keep our mesh size as 64×64 ; for $Ra = 10^9$, we keep our mesh size as 512×512 , and we compare the mean temperature profile with literature [77]. As seen in [Figure A.6](#), we get good agreement with the literature.

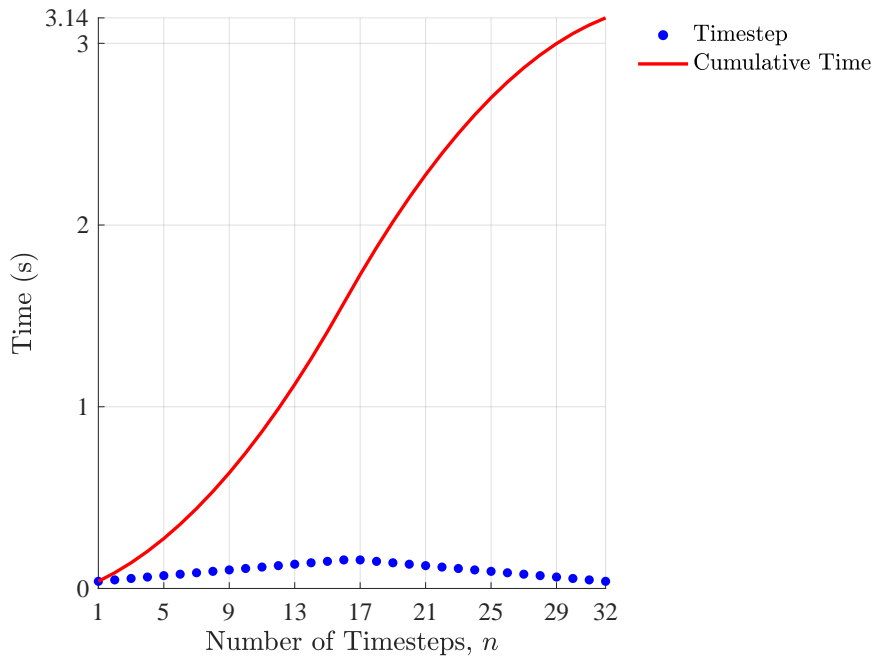


Figure A.2: Illustration of the variation in timestep during the MMS testing. The timestep increases linearly from $\frac{k}{4}$ to k , followed by a linear decrease from k to $\frac{k}{4}$, with $k = 0.157$. This pattern is shown in the figure, providing a graphical representation of the time step variation throughout the simulation.

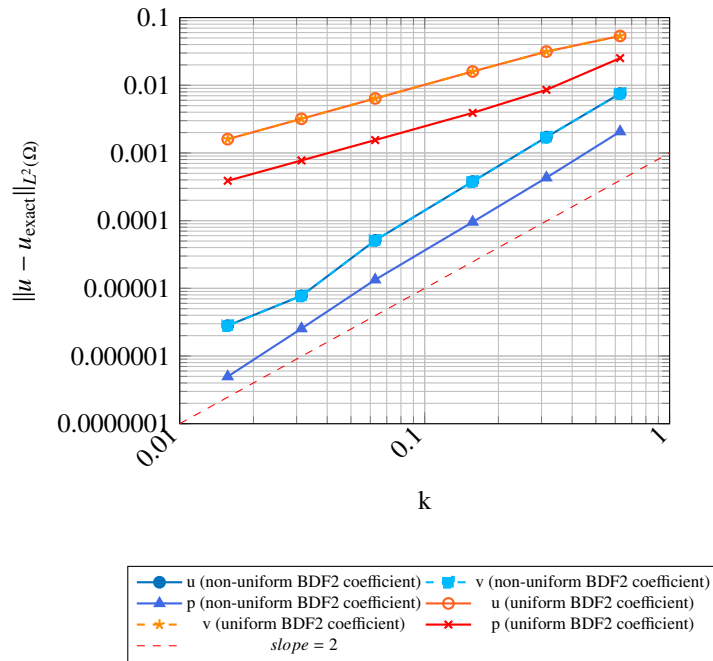


Figure A.3: Error norms for different BDF2 coefficients (Table 1) with varying levels of accuracy.

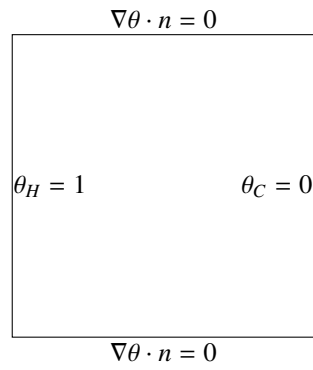


Figure A.4: Boundary condition settings for Rayleigh-Bénard.

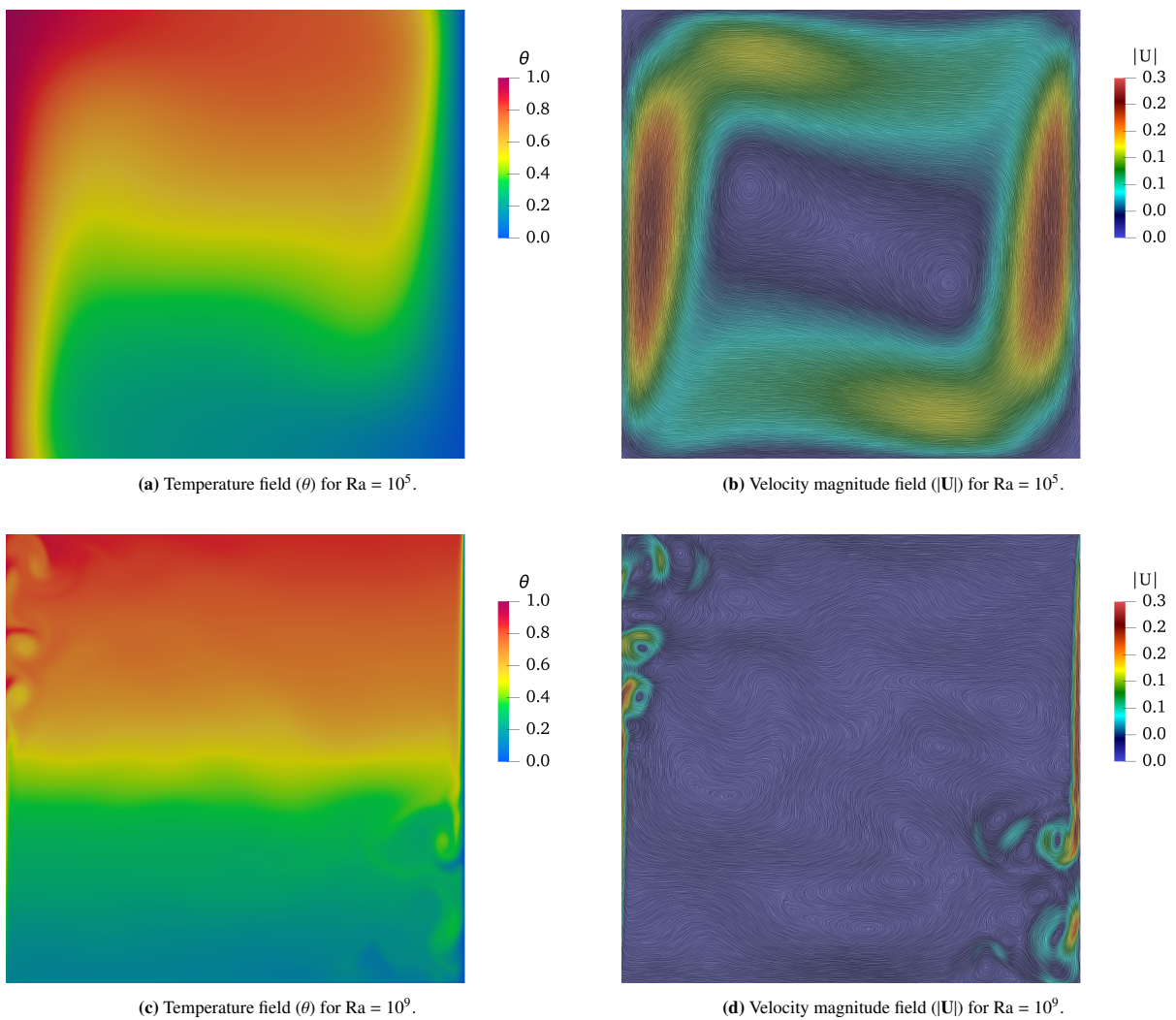


Figure A.5: Rayleigh-Bénard convection simulations for different Rayleigh numbers (Ra). The temperature field (θ) is shown on the left and the velocity magnitude field ($|U|$) is shown on the right. At lower Ra (10^5), the system exhibits steady convection, while at higher Ra (10^9), the system shows turbulent behavior with well-defined plumes and vortices.

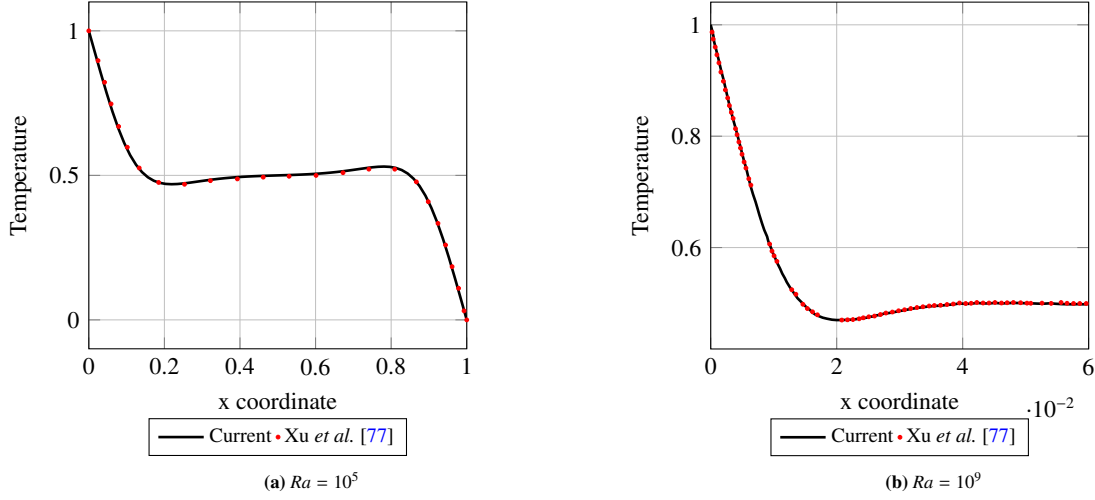


Figure A.6: 2D results for mean temperature profile.

Appendix B. Heuristic derivation of SBM formulation for Navier-Stokes

Appendix B.1. Derivation for Nitsche's method for Navier-Stokes

Nitsche's method starts with the Lagrange multiplier method and adds a penalty term to obtain the augmented Lagrangian formulation. We begin with the Lagrange multiplier method, which is given by:

$$\underbrace{\int w \lambda \, d\Gamma}_{\text{consistency term}} + \underbrace{\int \delta \lambda (u - u_D) \, d\Gamma}_{\text{adjoint-consistency term}}. \quad (\text{B.1})$$

After adding the penalty term $\beta \int w(u - u_D) \, d\Gamma$, we can obtain Nitsche's method:

$$\underbrace{\int w \lambda \, d\Gamma}_{\text{consistency term}} + \underbrace{\int \delta \lambda (u - u_D) \, d\Gamma}_{\text{adjoint-consistency term}} + \underbrace{\beta \int w(u - u_D) \, d\Gamma}_{\text{penalty term}}. \quad (\text{B.2})$$

Our objective is to determine the Lagrange multiplier, λ , for the Navier-Stokes equation. This is achieved by ensuring that the consistency term matches the boundary term, which arises when integration by parts is applied to the weak form of the Navier-Stokes equation. To derive the weak form, we start from the strong form of the Navier-Stokes equation and utilize test functions w and q :

$$\begin{cases} \rho \left(\frac{\partial u}{\partial t} + u \cdot \nabla u - f \right) - \nabla \cdot \sigma = 0 \\ \nabla \cdot u = 0 \end{cases} \Rightarrow \int w \rho \left(\frac{\partial u}{\partial t} + u \cdot \nabla u - f \right) \, d\Omega - \underbrace{\int w \nabla \cdot \sigma \, d\Omega}_{\text{Cauchy stress term}} + \int q \nabla \cdot u \, d\Omega = 0. \quad (\text{B.3})$$

Performing integration by parts (Section Appendix B.2) on the Cauchy stress term, we obtain the following:

$$-\int w \nabla \cdot \sigma \, d\Omega = \underbrace{\int \nabla w : \sigma \, d\Omega}_{\text{volume term}} - \underbrace{\int w \sigma \cdot n \, d\Gamma}_{\text{boundary term}}. \quad (\text{B.4})$$

The boundary term is the same as the consistency term in Nitsche's formulation so that we can obtain the following:

$$\int w \lambda \, d\Gamma = - \int w \sigma \cdot n \, d\Gamma \Rightarrow \lambda = -\sigma \cdot n = -(2\mu \nabla^s u - pI) \cdot n. \quad (\text{B.5})$$

And, we can obtain $\delta \lambda = -(2\mu \nabla^s w + qI) \cdot n$.

Upon substitution of λ and $\delta \lambda$ into equation Eq. B.2, Nitsche's formulation for Navier-Stokes can be obtained, and is expressed as follows:

$$-\underbrace{\int w(2\mu \nabla^s u - pI) \, d\Gamma}_{\text{consistency term}} - \underbrace{\int (2\mu \nabla^s w + qI)(u - u_D) \, d\Gamma}_{\text{adjoint-consistency term}} + \underbrace{\beta \int w(u - u_D) \, d\Gamma}_{\text{penalty term}}. \quad (\text{B.6})$$

To better satisfy the inflow boundary conditions, we include an additional term on Γ^- that represents the inflow segment of Γ ($\Gamma^- = x|u \cdot n < 0, \forall x \in \Gamma$):

$$-\underbrace{\int w(2\mu \nabla^s u - pI) \, d\Gamma}_{\text{consistency term}} - \underbrace{\int (2\mu \nabla^s w + qI)(u - u_D) \, d\Gamma}_{\text{adjoint-consistency term}} + \underbrace{\beta \int w(u - u_D) \, d\Gamma}_{\text{penalty term}} - \int w(u \cdot n)(u - u_D) \, d\Gamma^-. \quad (\text{B.7})$$

Appendix B.2. Integration by part for Cauchy stress term

Doing integration by part for the Cauchy stress term in Eq. B.3, we write the term in the form of Einstein notation so that it is easier to calculate:

$$\begin{aligned} & - \int w \nabla \cdot \sigma \, d\Omega = - \int w_i \frac{\partial \sigma_{ik}}{\partial x_k} \, d\Omega = - \int w_i \left(\mu \frac{\partial \varepsilon_{ik}}{\partial x_k} - \delta_{ik} \frac{\partial p}{\partial x_k} \right) \, d\Omega = - \int w_i \left(\mu \frac{\partial \varepsilon_{ik}}{\partial x_k} - \frac{\partial p}{\partial x_i} \right) \, d\Omega \\ & = \int \left(\underbrace{-\mu \frac{\partial (w_i \varepsilon_{ik})}{\partial x_k}}_{\text{term 1}} + \underbrace{\mu \varepsilon_{ik} \frac{\partial w_i}{\partial x_k}}_{\text{term 2}} + \underbrace{\frac{\partial (p w_i)}{\partial x_i}}_{\text{term 1}} - \underbrace{p \frac{\partial w_i}{\partial x_i}}_{\text{term 2}} \right) \, d\Omega = \int \left(\underbrace{-\mu \frac{\partial (w_i \varepsilon_{ik})}{\partial x_k} + \frac{\partial (p w_i)}{\partial x_i}}_{\text{term 1}} \right) \, d\Omega + \int \left(\underbrace{\mu \varepsilon_{ik} \frac{\partial w_i}{\partial x_k} - p \frac{\partial w_i}{\partial x_i}}_{\text{term 2}} \right) \, d\Omega \\ & = \int w_i (-\mu \varepsilon_{ik} n_k + p n_i) \, d\Gamma + \int \frac{\partial w_i}{\partial x_k} (\mu \varepsilon_{ik} - p \delta_{ik}) \, d\Omega = \int w_i (-\sigma_{ik} n_k) \, d\Gamma + \int \frac{\partial w_i}{\partial x_k} \sigma_{ik} \, d\Omega \\ & = - \int w \sigma \cdot n \, d\Gamma + \int \nabla w : \sigma \, d\Omega. \end{aligned} \quad (\text{B.8})$$

Appendix B.3. SBM for Navier-Stokes

In SBM, instead of enforcing boundary condition on the true boundary (Γ), we enforce Nitsche's method on the surrogate boundary ($\tilde{\Gamma}$) by changing the boundary condition from u_D to \tilde{u}_D :

$$-\underbrace{\int w(2\mu \nabla^s u - pI) \, d\tilde{\Gamma}}_{\text{consistency term}} - \underbrace{\int (2\mu \nabla^s w + qI)(u - \tilde{u}_D) \, d\tilde{\Gamma}}_{\text{adjoint-consistency term}} + \underbrace{\beta \int \tilde{w}(u - \tilde{u}_D) \, d\tilde{\Gamma}}_{\text{penalty term}} - \int w(u \cdot n)(u - \tilde{u}_D) \, d\tilde{\Gamma}^-. \quad (\text{B.9})$$

With Taylor expansion to account for the discrepancy between the surrogate and true boundary, the boundary

condition becomes $\tilde{u}_D = u_D - \nabla u \cdot d$. Substituting this expression into [Eq. B.9](#), we obtain:

$$\begin{aligned}
& - \underbrace{\int w(2\mu\nabla^s u - pI) d\tilde{\Gamma}}_{\text{consistency term}} - \underbrace{\int (2\mu\nabla^s w + qI)(u + \nabla u \cdot d - u_D) d\tilde{\Gamma}}_{\text{adjoint-consistency term}} \\
& + \beta \underbrace{\int (w + \nabla w \cdot d)(u + \nabla u \cdot d - u_D) d\tilde{\Gamma}}_{\text{penalty term}} - \int w(u \cdot n)(u + \nabla u \cdot d - u_D) d\tilde{\Gamma}^-.
\end{aligned} \tag{B.10}$$